Journal Name

ARTICLE TYPE

Cite this: DOI: 10.1039/xxxxxxxxxx

Prediction of low-field nuclear singlet lifetimes with molecular dynamics and quantum-chemical property surface†

Pär Håkansson*[a‡]

Received Date
Accepted Date

DOI: 10.1039/xxxxxxxxxx

www.rsc.org/journalname

Molecular dynamics and quantum chemistry methods are implemented to quantify nuclear spin-1/2 pair singlet-state relaxation rates for three molecular systems at low magnetic field and room temperature. Computational methodology is developed for weak interactions, particularly important for singlet states at low field. These include spin-rotation and spin-internal-motion effects, which describe the coupling of the spin-carrying nuclei to fluctuating local magnetic fields induced by the overall and internal molecular fluctuations, respectively. A high-dimensional tensor property surface using Kriging interpolation is developed to circumvent costly quantum-chemical calculations. Together with the intramolecular dipolar relaxation, all the simulated relaxation mechanisms are accounted for with a common theoretical framework. Comparison with experiment indicates that quantitative accuracy is obtained, sufficient to enable guidance in the molecular design of molecules with long-lived singlet order.

1 Introduction

Long-lived states (LLS) are configurations of nuclear spin systems that have decay time constants much longer than the conventional spin-lattice relaxation time (T_1) under ambient conditions [1–11]. The existence of such states creates many new possibilities in nuclear magnetic resonance (NMR) and magnetic resonance imaging (MRI) experiments, including the study of slow transport processes such as slow flow and diffusion [12], as well as the storage of hyperpolarized nuclear spin order for relatively long times [13,14].

Symmetry properties for the spin system provide a protection for long-lived states against common relaxation mechanisms [7]. For example, in systems of spin-1/2 pairs, the LLS known as *singlet order* is protected against motional fluctuations in the intramolecular dipole-dipole coupling between the members of the spin pair, which is often the dominant mechanism for T_1 [15]. In favourable cases, this allows the lifetime of singlet order, denoted T_S, to exceed T_1 by a large factor. Recently, a molecular system was designed which displays singlet relaxation time T_S exceeding 1 hour in a room-temperature solution, which is approximately 50 times longer than the conventional T_1 relaxation time [15,16]. This design [15] was in part guided by the type of calculation procedures detailed in this work.

The relaxation of LLS is caused by spin-symmetry breaking mechanisms and the most common ones are at least qualitatively well-understood. In cases of rigid molecular geometry, standard techniques based on Abragam-Redfield relaxation theory may be used to analyze nuclear dipole-dipole (DD) interactions and to predict molecular geometries that support LLS with long lifetimes [17–20]. In strong magnetic fields, chemical shift anisotropy (CSA) often dominates the relaxation of nuclear singlet order. Fast molecular tumbling, compared to both the CSA interaction and the nuclear Larmor frequency, gives rise to a quadratic dependence of T_S^{-1} on the magnetic field strength [19,21,22]. One unusual feature of the CSA mechanism of singlet relaxation is that the antisymmetric (rank-1) components of the CSA tensor often dominate [19].

In many cases the longest nuclear singlet relaxation times are encountered at low magnetic field, where the CSA mechanism is absent. The low-field regime is also of practical importance for the possibility of transport of the hyperpolarized medium finished with spin order from the polarization equipment to the site of use (an NMR spectrometer or MRI instrument). Plausible mechanisms to relax nuclear spin systems at low magnetic fields are the intramolecular dipole-dipole and spin-rotation (SR) mechanisms, as well as through intermolecular interactions with nuclear spins on solvent molecules, and paramagnetic species. When intermolecular interactions are minimized by suitable sample prepa-

[a] School of Chemistry, University of Southampton, SO17 1BJ Southampton, UK
‡ Present address: NMR Research Unit, P.O. Box 3000, FIN-90014 University of Oulu, Finland Tel: +358 (0)40 3531781; E-mail: nils.hakansson@oulu.fi

† Electronic Supplementary Information (ESI) available: [Details on the estimation of translational diffusion for the various solvents, $T_1^{-1}[CSA]$ for molecule **III** both from MD simulation, as well as the selection of internal regions for molecule **III**.]. See DOI: 10.1039/b000000x/

ration (solvent deuteration and elimination of paramagnetic impurities) the intramolecular mechanisms dominate. With the assumption of perfectly rigid molecules, the intramolecular contributions to nuclear singlet relaxation from out-of-pair DD couplings and spin-rotation couplings are readily estimated. However, in most cases, such treatments predict nuclear singlet lifetimes that are orders of magnitude longer than experimental measurements of T_S. The discrepancies are too large to be accounted for by uncertainties in the theory, or by small intermolecular interactions.

Spin-rotation interactions involve the coupling of nuclear spins with small fluctuating magnetic fields generated by the rotation of molecules in solution. Since the positive and negative electrical charges are not located at the same places in a molecule, molecular rotation generates local currents that are associated with local magnetic fields and these couple to the magnetic nuclei. In the *SR* context one typically considers the overall (end-over-end) rotation of a rigid molecules subjected to frequent collisions. There is much early literature on the spin-rotation mechanism for small molecules, especially in the gas phase[23–27], where in most cases, the molecules are approximated as rigid rotating bodies, subject to collisions and hydrodynamic forces[25]. This approach has also been used for singlet relaxation[21,28,29]. Unfortunately the rigid-body approach greatly underestimates nuclear singlet relaxation rate in most realistic cases. This is unsurprising since most molecules are highly flexible; even if the overall rotation of a medium-sized molecule in solution is sluggish, the internal motion may be considerable, and may include torsions and twists that have much in common with rotational motion.

The effect of internal motion on nuclear spin relaxation has been examined for the special case of rotating methyl (CH_3) groups[30–34]. However, we find that also other types of internal molecular flexibility have a significant effect on nuclear spin relaxation, even when the molecule contains no obvious rotating parts such as methyl groups. An important part of this work is a method for calculating the effect of local internal molecular motion on nuclear singlet relaxation. We call this the *spin-internal-motion* (*SIM*) mechanism of nuclear singlet relaxation, distinct from the *spin-rotation* mechanism (*SR*), which only refers to the effect of overall molecular rotation, and which is usually negligible, except for very small molecules. It is shown in the present and previous work[15] that the *SIM* mechanism, on the other hand, can dominate T_S at low field, especially for large, flexible molecules.

To arrive at a valid general discussion of *SIM* and *SR* T_S relaxation, the time dependence of the interaction tensors are needed, based on atomistic molecular dynamics (MD) simulations. Typically this leads to a massive computational bottleneck in quantum chemistry (QC) calculations since QC information is required at sub-picosecond resolution for the nanosecond long MD trajectories. The current paper has two main ambitions, first, to provide a general computational framework to address the costly quantum chemistry calculations required for NMR relaxation and, secondly, to describe the details required in predicting intramolecular nuclear singlet relaxation mechanisms at low magnetic field.

The method described here for the computation of the singlet relaxation time T_S combines (MD) simulations with a QC-property surface (QCPS), allowing for calculation of the simulated snapshots in a cost-efficient way. This provides the first framework for MD-QC singlet-state calculations without adjustable parameters. The work also sets the foundation for forthcoming work on additional mechanisms.

The combination of MD and QC calculations has been used before for T_1 studies of paramagnetic agents[35–38] and quadrupole relaxation[39] using various approaches. For instance, for paramagnetic agents, the relevant (zero-field splitting) QC tensor is modelled within a truncated normal mode expansion, limiting the model to small spatial deviations of the nuclei[35]. Different possibility is seen for is a low-density Xe gas, where the approximate pairwise additive approximation reduces the computational cost of QC-tensors as the instanteneous interactions are computed with a parameterized one-dimensional "NMR-force field"[36] and thus not restricted to small-amplitude spatial motion. The limitation of a normal mode expansion as well as restriction to a low dimensional parameterization is overcome in the Refs.[37–40], where the QC-tensors are explicitly calculated for each MD snapshot, thus allowing for all the motional modes of the system to be incorporated. However, a limitation is the computational bottleneck discussed above or, alternatively, the large statistical error (see for instance Figure 2 in Ref.[39]).

To progress in the area of modelling LLS systems, we address in this work two main complexities, 1) the computational challenges in the QC-computed tensors of the spin Hamiltonian that need to be sampled from a MD trajectory snapshots and 2) introduce the *SIM* concept and adapt it to MD simulations. The latter addresses, in particular, the question of how to progress from an approach where, for instance, CH_3 is *postulated* as causing spin-internal relaxation[30,31] towards a procedure where the most relevant internal region is *predicted* from the MD simulation.

In the present work, the QC-tensor computational cost bottleneck is overcome by using a spatial interpolation scheme. In particular, we explore the powerful Kriging model[41] (also referred to as Gaussian Process or DACE: design and analysis of computer experiments), widely used in the computational engineering community[41–43], and recently also for computational chemistry. The Kriging interpolation scheme was found to be the most efficient in a comparison of polarisable water models[44]. A Kriging model is used in the global line-shape fitting procedure for an electron spin resonance spectrum, for achieving a necessary reduction of the number of function evaluations[45]. In this work we precent, for the first time, Kriging MD/QC NMR relaxation studies. Briefly, a training set of instantaneous molecular configurations are selected and the QC-tensors are computed; subsequently, a Kriging model is parameterized from the QC outputs[41]. The model achieved in this way provides a QCPS that replaces the costly QC snapshot calculations in the analysis of the MD simulation. QCPS is analogous to the MD-force field that can be thought of circumventing the costly QC force calculations when performing conventional MD-simulations. The underlying Bayesian assumption behind the Kriging model is particularly valuable since, in addition to providing the QCPS, it also provides a model estimate of the error[41]. This may be used for a cost-efficient update of the

training set.

Before any useful estimates can be made from the Kriging model, a reasonable first training set of configurations is required. Setting up the first small training set poses a challenge due to the complicated parameter space in MD simulations, with generally very many, both intra-and intermolecular degrees of freedom, which cause that the commonly used efficient space-filling method developed in computational engineering[41] for this purpose cannot be directly applied. To overcome this, a space-filling method that is new to the quantum chemistry community is provided, which works directly with the available set of MD snapshots. Hence, presented is a QCPS methodology, which is expected to find a wide set of applications well beyond NMR relaxation.

The paper is organised as follows. After a review of the molecular systems studied in section 2, the section 3 provides the background for the relaxation rate calculations. The derivation of *SR*, *SIM* and *DD* Hamiltonians is given in section 4, and in section 5, the specific form of the time correlation functions (TCFs) are discussed, followed by, in section 6, a survey of the implementation of the Kriging model in the context of NMR relaxation. The results are discussed in section 7 and conclusions drawn in section 8.

2 Molecular systems

Three molecular systems with relaxation parameters measured in previous works are considered, two ^{13}C-labeled molecules[19] and ^{15}N-nitrous oxide[28]. Singlet relaxation in these systems has a long decay constant (T_S), for which a complete theoretical understanding is lacking, making these interesting test molecules. To access the low-field (approximate) singlet state for these systems, pulse-sequence and field-cycling are, respectively, employed, detailed in Refs.[19,28]. A small chemical shift difference is needed to access the singlet state at high field (> 1 Tesla), and a suitable pulse sequence depends on the degree of strong coupling (relating spin-spin coupling to chemical shift), making these parameters interesting to present. The molecular structures and relaxation rates are provided in Figure 1.

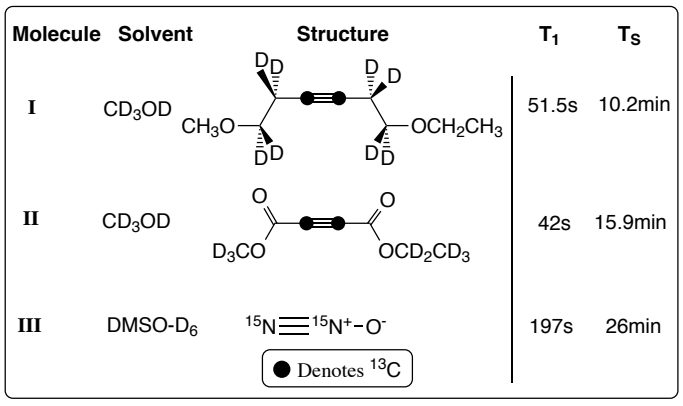

Fig. 1 The molecular structures and the experimental room temperature relaxation parameters of the three LLS-candidates studied at 2.2 mT magnetic field.

Sample I: (Figure 1,**I**) 1-Ethoxy-6-methoxyhex-3-yne-3,4-$^{13}C_2$-1,1,2,2,5,5,6,6-d_8 is a molecule synthesized with the aim at at the stability of the singlet state at high magnetic field. The synthesis steps are given in the ESI of Ref.[19], the difference in the isotropic chemical shift of the nuclei carrying the singlet state is ∼0.13 ppm, and the intra-pair J_{CC}-coupling is 180 Hz. All samples were degassed to remove molecular oxygen. Sample **I** dissolved in deuteromethanol has a singlet order decay time of T_S =10.2 min measured at 2.2 mT, approximately 12 times greater than T_1[19]. The singlet order decay time is of similar magnitude at high magnetic field (7 T)[19].

Sample II: (Figure 1,**II**) 1-Ethyl-4-methylbut-2-ynedioate-2,3-$^{13}C_2$-d_8 was synthesized as described in the Supporting Information of Ref.[19]. Sample **II**, dissolved in deuteromethanol, and degassed, has a singlet-order decay time of T_S =15.9 min (nearly 23 times T_1) at low magnetic field (2 mT)[19]. The difference in the isotropic chemical shift is ∼0.62 ppm and the J_{CC}-coupling equals 185 Hz. Sample **II** has a singlet-order life time similar to T_1 at high magnetic field (7 T)[19]. Hence, to observe a significantly prolonged singlet-order lifetime, a lower magnetic field is required.

Sample III: (Figure 1,**III**) $^{15}N_2O$ gas is dissolved in the degassed DMSO-d_6 solvent to a concentration of about 0.3 M in Ref.[28]. The difference in the isotropic chemical shift is circa 82 ppm and the J_{NN}-coupling 8.1 Hz. The singlet-order decay time T_S =26 min is reported at 2.2 mT field Ref.[28] (eight times T_1). The inequivalent nuclei require a low-field relaxation measurement.

3 Relaxation theory

The relaxation of singlet order and magnetisation is studied for a quantum spin system (I) coupled to a classical "lattice" (L) (also denoted thermal bath), where the lattice degrees of freedom are explicitly obtained through MD simulations. The relaxation rates are treated within a perturbative form of the Liouville-von Neumann equation[46,47]. A perturbative form is motivated by the fact that the molecular lattice degrees of freedom have much faster modulation than the spin-lattice (IL) coupling strength, hence the studied systems are in the motional narrowing or Redfield regime. In this context, the spin dynamics is governed by the Bloch-Wangsness-Redfield (BWR) master equation:

$$\frac{d\rho(t)}{dt} = [-i\hat{H}^I + \hat{\Gamma}^{IL}]\rho(t), \tag{1}$$

where $\rho(t)$ is the density matrix of the spin degrees of freedom (trace taken over the lattice degrees), $\hat{H}^I$ and $\hat{\Gamma}^{IL}$ are the coherent and relaxation superoperators, respectively[47]. The relaxation superoperator accounts for the modulation of the spin system by the lattice degrees of freedom, causing the relaxation of the spin states, and is given by

$$\hat{\Gamma}^{IL} = \sum_{\lambda,\lambda'} \hat{\Gamma}^{\lambda,\lambda'}, \tag{2}$$

where $\lambda \in \{SR, SIM, CSA, DD, iDD, sDD, SR2K, pDD, \dots\}$ and the individual relaxation mechanisms (with $\lambda = \lambda'$), as well as cross-correlations ($\lambda \neq \lambda'$) may be included. Some of the plausible relaxation mechanisms[48] are, besides the already mentioned *SR* and *SIM*, chemical shift anisotropy (*CSA*), in-pair (*DD*), the remaining intramolecular (*iDD*) and the solvent (intermolec-

ular, *sDD*) dipole-dipole coupling, scalar relaxation of second kind (*SR*2*K*), and hyperfine coupling to paramagnetic impurities (pDD). The relaxation supermatrix elements are formed by[47]

$$\Gamma^{\lambda,\lambda'}_{rsuv} = \frac{1}{2}[J^{\lambda,\lambda'}_{rusv}(\omega_{ru}) + J^{\lambda,\lambda'}_{rusv}(\omega_{vs}) - \delta_{sv}\sum_{\gamma} J^{\lambda,\lambda'}_{r\gamma v\gamma}(\omega_{\gamma u}) - \delta_{ru}\sum_{\gamma} J^{\lambda,\lambda'}_{v\gamma s\gamma}(\omega_{v\gamma})], \tag{3}$$

where

$$J^{\lambda,\lambda'}_{rsuv}(\omega) = \int_0^{\infty} G^{\lambda,\lambda'}_{rsuv}(\tau)\exp(-i\omega\tau)d\tau, \tag{4}$$

$$G^{\lambda,\lambda'}_{rsuv}(\tau) = \left(|r\rangle\langle s|\overline{H^{\lambda}(t)H^{\lambda'}(t+\tau)}|u\rangle\langle v|\right). \tag{5}$$

Here the states $\{|r\rangle,|s\rangle,\dots\}$ are the eigenstates of the spin-lattice Hamiltonian $H^{\lambda}(t)$, the Liouville bracket[46] for superoperator A is defined as $(X|A|Y) = Tr_I\{X^{\dagger}AY,\rho\}/Tr_I\{X^{\dagger}Y,\rho\}$, the overbar ($\overline{\{\cdot\}}$) denotes an ensemble average over the lattice degrees of freedom, and $J^{\lambda,\lambda'}_{rsuv}(\omega)$ is a spectral density. Eqn (5) introduces the spin-lattice TCF, which is central to this work. In particular the spin-Hamiltonian trajectories are computed from MD simulations. The main aim of this paper is to provide an efficient methodology for the ensemble average in eqn (5) to be estimated from first principles.

The study focuses on low magnetic-field experiments and the corresponding, important relaxation mechanisms, *SIM*, *SR*, *DD* and *iDD*. Considering the specific sample preparation procedures (see sec. 2), the solvent effects (*sDD* and *pDD*) have minor influence and will be discussed in forthcoming work. Due to a timescale separation of the molecular reorientation (modulating *DD* and *iDD* at pico- to nanosecond timescale in this work) and collisions (modulating *SIM*, *SR* at a femto- to subpicosecond timescale), motivates omitting the cross-correlations between these two mechanisms.

The relevant TCFs [*cf.* eqn (5)] are compactly represented as the zero-quantum block of the Liouville matrix (thus excluding the non-secular terms):

$$G^{\lambda}_{S_0S_0}(\tau) = \left(S_0|\overline{H^{\lambda}(t)H^{\lambda}(t+\tau)}|S_0\right) \tag{6}$$

$$G^{\lambda}_{I_{jz}I_{jz}}(\tau) = \left(I_{jz}|\overline{H^{\lambda}_j(t)H^{\lambda}_j(t+\tau)}|I_{jz}\right), \tag{7}$$

where the population superoperators[8] $S_0 \propto \boldsymbol{I}_j\cdot\boldsymbol{I}_k$ (also denoted T^{jk}_{00}, $\boldsymbol{I}_k$ is the nuclear spin operator for spin k) and I_{jz} are introduced for the singlet and longitudinal relaxation of spin j, respectively. Next, the specific form of *SR* and *SIM* Hamiltonians is discussed, after which the form of the TCFs of eqs (6,7) are discussed, in sections 5 and 6.

4 Spin-rotation (*SR*) and Spin-Internal-Motion (*SIM*) Hamiltonian

In 1967, Dubin and Chan[30] extended the concept of spin-rotation interaction and considered the additional relaxation mechanism caused by the internal rotation of a CF_3 group. The theory for this process has been discussed for instance by Bull[31] and Lee[32] considering a symmetric internal top[49]. In this work, we generalise this concept and consider not only the internal *rotation* but all the motions that may induce a local magnetic field, for instance internal torsional motion, in an important relaxation pathway denoted spin-internal-motion (*SIM*).

The *SR* Hamiltonian accounts for the magnetic field induced by the *overall rotation* of nuclei and electrons around the nucleus of interest. This magnetic field is expected to arise from from two main effects[32]: (i) electrons do not perfectly follow the nuclear framework, for instance they lag behind, causing a net current and (ii), even with electrons following the nuclear framework exactly, the nuclear and electronic charge distributions do not cancel out, thus they give rise to net atomic charges ("partial charges"). The *SR* interaction Hamiltonian[25] has the form

$$H^{SR}(t) = \sum_{k=1}^{K} \boldsymbol{I}_k\cdot\boldsymbol{C}^{SR}_k\cdot\boldsymbol{J}(t), \tag{8}$$

where $\boldsymbol{C}^{SR}_k$ is the spin-rotation tensor per unit angular momentum and $\boldsymbol{J}(t)$ is the overall (molecular) angular momentum. For *SR*, the molecule is considered (approximately) rigid. To compute $\boldsymbol{C}^{SR}_k$, the first effect (i) requires a quantum chemistry treatment where the deviation from the Born-Oppenheimer approximation is accounted for at perturbation level of theory (see Ref.[50], p 337). The necessary details of *SR* tensor calculation are noted in sec. 6.2. In this work, we restrict the discussion to ambient-temperature liquids and dense gases, where a classical treatment of $\boldsymbol{J}(t)$ is sufficient, allowing classical MD simulations to be used (see sec. 6.1). With classical angular momentum, eqn (8) represents a hermitian operator and a symmetrized SR-Hamiltonian[51] is not required.

The *SR* interaction is concerned with a rigid molecular geometry and the presence of internal dynamics is not explicitly accounted for. In particular for a large molecule, the overall *SR* interaction has only a minor contribution to relaxation. On the other hand, fluctuations of a region of atoms in the vicinity of the spin of interest may provide a significant relaxation mechanism. Working with angular velocity is more convenient than with angular momentum in the following discussion, as well as in the final numerical implementation. We work with one internal region in close proximity to each spin, as discussed below. The local nuclear fluctuations [$\Delta\boldsymbol{r}(t)$] require that the basic effects (i) and (ii) are accounted for with a time dependent tensor $\boldsymbol{C}_k[\Delta\boldsymbol{r}(t)]$, defined per unit angular velocity, and the local angular velocity $\dot{\boldsymbol{\theta}}(t)$ (bending, torsions etc. with the dot denoting time derivative) for the internal region (*cf.*, Figure 2). The combined *SR* and *SIM* interactions assume in this work a form similar to eqn (54) in Ref.[31], except with a time-dependent tensor

$$H^{SR}(t) + H^{SIM}(t) = \sum_{k=1}^{K} \boldsymbol{I}_k\cdot\{\boldsymbol{C}^{e}_k\cdot\boldsymbol{\omega}^{e}(t) + \boldsymbol{C}_k[\Delta\boldsymbol{r}(t)]\cdot\dot{\boldsymbol{\theta}}_k(t)\}, \tag{9}$$

where the *SR* interaction of eqn (8) is accounted for with interaction $\boldsymbol{C}^{e}_k$ (per unit angular velocity) and the overall angular velocity $\boldsymbol{\omega}^{e}$ of the rigid equilibrium frame, denoted by superscript e.

Clearly more than one region associated with each spin may be flexible and eqn (9) is thus an approximation that may be generalised to several internal regions. The final result will be

presented for *one* region per spin, to avoid increased computational complexity. This is motivated by noting that additional internal regions, by necessity located further away from the spin k, have a drastically reduced relaxation contribution. Hence, the additional remote regions behaves as rapidly fluctuating magnetic dipoles with r^{-6} relaxation rate dependence on the distance r between the region and NMR nucleus. To motivate this approximation, order-of-magnitude estimates with additional regions are discussed in sec 6.4.

4.1 Angular velocity for flexible molecules

To discuss the angular velocity, the classical kinetic energy is a useful starting point. The instantaneous position of nucleus l may, on one hand, be expressed relative to a space-fixed system of axes (that we will call the laboratory frame), as well as in the molecular centre-of-mass (MCM) frame, which is shown in Figure 2(A). This position vector is denoted

$$\mathbf{r}_l = x_l\mathbf{e}_x + y_l\mathbf{e}_y + z_l\mathbf{e}_z, \tag{10}$$

where the unit vectors $\{\mathbf{e}_i\}$ are along the cartesian axes of the molecule-fixed frame. It is useful to relate the instantaneous position vector to the *equilibrium* position $\{\mathbf{r}_l^e\}$ via

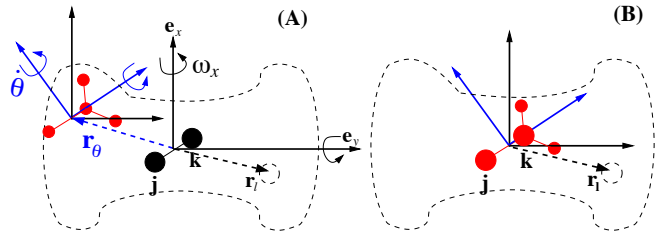

Fig. 2 Illustrations of molecule (dashed line) with a singlet spin pair (j,k) and internal region (red nuclei). In panels **A** and **B**, centers of mass of the molecule and the region are displaced ($\mathbf{r}_\theta$) and coincide, respectively.

$$\Delta\mathbf{r}_l = \Delta x_l\mathbf{e}_x + \Delta y_l\mathbf{e}_y + \Delta z_l\mathbf{e}_z,$$

where $\Delta x_l = x_l - x_l^e$, etc. The velocity in the laboratory frame of the nucleus l, written in terms of the angular velocity of the molecule-fixed frame ($\boldsymbol{\omega}$), is [52]

$$\mathbf{v}_l = \boldsymbol{\omega}\times\mathbf{r}_l + \mathbf{u}_l \tag{11}$$

where the internal velocity is $\mathbf{u}_l = \dot{\Delta\mathbf{r}}_l = \dot{\mathbf{r}}_l$, and the last equality follows from $\{\dot{\mathbf{r}}_l^e \equiv \mathbf{0}\}$.

The kinetic energy ($T = \frac{1}{2}\sum_l m_l\mathbf{v}_l^2$) relative to the MCM is given in [52]

$$2T = \sum_{l=1}^{N} m_l(\boldsymbol{\omega}\times\mathbf{r}_l)\cdot(\boldsymbol{\omega}\times\mathbf{r}_l) + \sum_{l=1}^{N} m_l u_l^2 + 2\boldsymbol{\omega}\cdot\sum_{l=1}^{N} m_l\mathbf{r}_l\times\mathbf{u}_l, \tag{12}$$

where the contributions from the left are: the overall molecular tumbling, internal dynamics (vibrations, torsions), and the coupling between the two processes, for a molecule containing N nuclei. The last term may be written as $\sum_l \mathbf{r}_l\times(m_l\mathbf{u}_l)$ to represent the total internal (vibrational) angular momentum. The degree by which this is coupled to the overall molecular tumbling (*i.e.*, $\boldsymbol{\omega}$) may be minimized by our choice of the molecular frame.

4.1.1 Eckart frame

We choose the molecular frame $\{\mathbf{e}_i\}$ as the Eckart frame [53,54] (EF) that is determined, for a polyatomic molecule, by three quantities: the nuclear masses m_l, as well as their instantaneous and equilibrium positions, $\{\mathbf{r}_l(t)\}$ and $\{\mathbf{r}_l^e\}$, respectively. Although the initial orientation of the EF (the choice of $\{\mathbf{r}_l^e\}$) can be chosen at random relative to the laboratory frame, the Eckart conditions [54] are needed to construct the subsequent frames. The Eckart conditions find the molecule-fixed frame that minimizes the coupling between the total molecular vibration and rotation, and read as

$$\sum_l m_l\mathbf{r}_l^e\times\mathbf{r}_l(t) = \mathbf{0}. \tag{13}$$

The EF is an orthonormal right-handed triad of three Cartesian vectors constructed such that eqn (13) is fulfilled [54]. Briefly, first a set of Eckart vectors $\mathbf{E}_i = \sum_{l=1}^{N} m_l r_{l,i}^e\mathbf{r}_l$ are computed for $i = x,y,x$. Secondly, the $\boldsymbol{E}_i$ are orthonormalized by $[\mathbf{e}_x,\mathbf{e}_y,\mathbf{e}_z] = [\mathbf{E}_x,\mathbf{E}_y,\mathbf{E}_z]\mathbf{E}^{-1/2}$, employing the (3×3) Gram matrix $\mathbf{E}$ (elements $E_{xy} = \mathbf{E}_x\cdot\mathbf{E}_y$, etc.). Effectively, the Eckart conditions ensure that the angular momentum contribution of the molecule-fixed system $\{\mathbf{r}_l^e\}$ is zero if $\{\mathbf{r}_l(t)\}\to\{\mathbf{r}_l^e\}$ for vectors expressed in the EF, and in this particular case, the molecule rotation is decoupled from the internal motion. In the general case, a perfect decoupling cannot be achieved [54]. Since the molecular moment of inertial axis frame may deviate from the EF (see sec 10.2.1 in Bunker and Jensen [55] for an illustrative example), the EF is a suitable choice for flexible molecules.

The kinetic energy using the Eckard condition (eqn (13)) is obtained from

$$2T = \boldsymbol{\omega}^T(t)\cdot\mathbb{I}(t)\cdot\boldsymbol{\omega}(t) + \sum_{l=1}^{N} m_l u_l^2(t) + 2\boldsymbol{\omega}(t)\cdot\sum_{l=1}^{N} m_l\Delta\mathbf{r}_l(t)\times\mathbf{u}_l(t), \tag{14}$$

where ^{T} denotes transpose and the first term in eqn (12) is rewritten in terms of the components of the instantaneous moment of inertia [52] $[\mathbb{I}(t)]$,

$$I_{ab} = \sum_{l=1}^{N} m_l\left(\delta_{ab}r_l^2 - r_{l,a}r_{l,b}\right), \quad a,b\in\{x,y,z\}. \tag{15}$$

4.1.2 Overall and internal angular velocity

We are interested in the coupling between the overall motion and one flexible region per spin required in eqn (9), leading to the (simplified) kinetic energy expression of eqn (14), where the region consists of K nuclei. We will return to the topic of defining an internal region for each nucleus, in sec. 6.4.

To define an internal angular velocity it is assumed that, during a (possibly very short) time interval, the nuclei in the internal region move in concert and, if for simplicity the center of mass coincides with the MCM (Figure 2**B**), the kinetic energy is

$$2T = \boldsymbol{\omega}^T(t)\cdot\mathbb{I}(t)\cdot\boldsymbol{\omega}(t) + \dot{\boldsymbol{\theta}}^T(t)\cdot\mathbb{I}_\theta(t)\cdot\dot{\boldsymbol{\theta}}(t) + 2\boldsymbol{\omega}^T(t)\cdot\mathbb{I}_\theta(t)\cdot\dot{\boldsymbol{\theta}}(t), \tag{16}$$

where $\dot{\boldsymbol{\theta}}(t)$ is the angular velocity of the region relative to the molecular frame, and $\mathbb{I}_\theta$ is the corresponding moment of inertia

(computed with eqn (15) for the relevant K nuclei). The overall and internal angular momenta relative to the MCM are given by $J_a = \partial T/\partial \omega_a$ and $j_\alpha = \partial T/\partial \dot{\theta}_\alpha$ respectively[52]:

$$\mathbf{J}(t) = \mathbb{I}(t)\cdot\boldsymbol{\omega}(t) + \mathbb{I}_\theta(t)\cdot\dot{\boldsymbol{\theta}}(t) \tag{17}$$

$$\mathbf{j}(t) = \mathbb{I}_\theta(t)\cdot\boldsymbol{\omega}(t) + \mathbb{I}_\theta(t)\cdot\dot{\boldsymbol{\theta}}(t). \tag{18}$$

For the more general case in which the center-of-mass of the internal region is displaced relative to the MCM (non-vanishing $\mathbf{r}_\theta$ in Figure 2A), the angular momenta are

$$\mathbf{J}(t) = \mathbb{I}(t)\cdot\boldsymbol{\omega}(t) + [\mathbb{I}_\theta(t) + \mathbb{I}_{r_\theta}(t)]\cdot\dot{\boldsymbol{\theta}}(t) \tag{19}$$

$$\mathbf{j}(t) = [\mathbb{I}_\theta(t) + \mathbb{I}_{r_\theta}(t)]\cdot\boldsymbol{\omega}(t) + [\mathbb{I}_\theta(t) + \mathbb{I}_{r_\theta}(t)]\cdot\dot{\boldsymbol{\theta}}(t), \tag{20}$$

where the additional $\mathbb{I}_{r_\theta}(t)$ is given by the parallel axis theorem[52] and denotes the moment of inertia of the center-of-mass of the region (eqn (15) computed with the single mass $m_\theta = \sum_l^K m_l$ and $\mathbf{r}_\theta$). From eqn (20) we obtain

$$\boldsymbol{\omega}(t) + \dot{\boldsymbol{\theta}}(t) = [\mathbb{I}_\theta(t) + \mathbb{I}_{r_\theta}(t)]^{-1}\mathbf{j}(t),$$

where the components of $\mathbb{I}_\theta(t), \mathbb{I}_{r_\theta}(t)$ and $\mathbf{j}(t) = \sum_l^K m_l \mathbf{r}_l \times \mathbf{v}_l$ are readily available from a MD simulation.

The components of the rigid-body *SR* and the *SIM* contributions are interesting to discuss individually. However, the available MD trajectory is for a completely flexible molecule. To separate these contributions, the rigid-body angular velocity is obtained by filtering out *conformation changes* and bond vibrations, by computing $\boldsymbol{\omega}^e(t) = (\mathbb{I}^e)^{-1}(t)\mathbf{J}^e(t)$ with $\mathbf{J}^e$, and $(\mathbb{I}^e)^{-1}$ obtained from the equilibrium geometry $\mathbf{r}^e$ accordingly rotated to the instantaneous EF. Note that the calculation of $\mathbf{J}^e$ is performed with the internal velocity contribution still present (see eqn (11)). However, this is of small amplitude compared to the overall molecular rotation and will be kept here, in favour of a simpler calculation. The angular velocity of the internal region is computed as the remainder

$$\dot{\boldsymbol{\theta}}(t) = [\mathbb{I}_\theta(t) + \mathbb{I}_{r_\theta}(t)]^{-1}\mathbf{j}(t) - \boldsymbol{\omega}^e(t), \tag{21}$$

containing the angular velocity of the internal region [*cf*. Figure 2A] and its coupling to the molecular angular velocity.

5 Spin states and relaxation rates

5.1 SR and *SIM* relaxation

Contributions to the magnetic field at the nucleus k are given by the definitions

$$\mathbf{B}_k^{SIM}(t) \equiv [\boldsymbol{C}_k(\boldsymbol{\Theta}(t))]^{Lab}\cdot\dot{\boldsymbol{\theta}}_k(t)$$

$$\mathbf{B}_k^{SR}(t) \equiv [C_k^e(\mathbf{r}^e)]^{Lab}\cdot\boldsymbol{\omega}^e(t),$$

where the internal molecular dynamics is expressed in the internal coordinate representation $\Delta\mathbf{r}(t) \to \boldsymbol{\Theta}(t)$. Both tensors have an additional time dependence due to the rotation from the instantaneous Eckart to laboratory frame [accomplished as $[\boldsymbol{C}_k]^{Lab}(t) = \mathbf{e}(t)\cdot[\boldsymbol{C}_k(\boldsymbol{\Theta}(t))]^{EF}\cdot\mathbf{e}^{-1}(t)$]. The TCFs are constructed[56] from eqs 6, 7 and 9:

$$G^\lambda_{S_0S_0}(\tau) = \frac{2}{3}\sum_{l=\{x,y,z\}}\overline{\Delta B_l^\lambda(t_0)\Delta B_l^\lambda(t_0+\tau)} \tag{22}$$

$$G^\lambda_{I_zI_z}(\tau) = \frac{1}{2}\sum_{\substack{i=j,k\\ l=\{x,y\}}}\overline{B^\lambda_{l,i}(t_0)B^\lambda_{l,i}(t_0+\tau)}, \tag{23}$$

where $\lambda = \{SIM, SR\}$, (j,k) denote the spin pair and $\Delta B_l^\lambda(t) = B_{j,l}^\lambda(t) - B_{k,l}^\lambda(t)$. Due to the sub-picosecond relaxation time corresponding to these TCFs, the relaxation rates (T_S^{-1}, T_1^{-1}) are available by direct numerical integration of $G^\lambda_{S_0S_0}(\tau)$ and $G^\lambda_{I_zI_z}(\tau)$, *i.e.*, in the extreme narrowing regime.

5.2 Intramolecular dipole-dipole relaxation

We consider the singlet nuclear spin pair (j,k) weakly coupled to additional spins q, hence the dipole-dipole and J-coupling fulfill the following relations: $\|H^{DD}_{jk}\| \gg \{\|H^{iDD}_{jq}\|, \|H^{iDD}_{kq}\|\}$ and $\|J_{jk}\| \gg \{\|J_{jq}\|, \|J_{kq}\|\}$, respectively. Thus the eigenstate of the singlet pair jk is approximately preserved, despite these external interactions[57].

The spin pair is influenced by a lattice that consists of additional q-spins, as well as the classical degrees of freedom (molecular tumbling and conformational changes). The relaxation properties of the spin pair are conveniently described with a composite lattice that consists of both the classical degrees and the q-spins. This approach is, for instance, followed in the derivation of paramagnetic relaxation enhancement[58]. The DD Hamiltonian, which is based on two spin operators, is formally rewritten in terms of single spin operators[59,60]:

$$H^{DD,iDD}(t) = \boldsymbol{I}_j\cdot\boldsymbol{B}^{DD}_{j,k}(t) + \sum_q[\boldsymbol{I}_j\cdot\boldsymbol{B}^{iDD}_{j,q}(t) + \boldsymbol{I}_k\cdot\boldsymbol{B}^{iDD}_{k,q}(t)], \tag{24}$$

where the $\boldsymbol{I}_j = (I^{1,j}_{-1}, I^{1,j}_0, I^{1,j}_1)$ are first-rank spin operators for nuclear spin j and $\boldsymbol{B}^{iDD}_{j,q}(t)$ is the dipolar field created by spin q at the site of j, which depends on the location of spins q. For the component l, the dipolar field as a first-rank operator reads

$$B^{(1)}_{l,j,q}(t) = c^{DD}_{jq}\sqrt{30}\sum_{n=-1}^{1}(-1)^n[C^{2,\,1,\,1}_{l-n,n,n-l}]I^{1,q}_n\frac{D^2_{0,l-n}[\Omega_{jq}(t)]}{r^3_{jq}(t)}, \tag{25}$$

where Ω_{jq} is the orientation of the internuclear axis between the spins j and q relative to the laboratory frame, r_{jq} is the corresponding distance, $D^{(2)}_{0,l-n}$ is a second-rank Wigner rotation matrix element, $c^{DD}_{jq} = \gamma_j\gamma_q\mu_0\hbar/4\pi$ (with symbols in their usual meaning), and $[C^{2,\,1,\,1}_{l-n,n,n-l}]$ are the appropriate 3j symbols[61]. Non-equivalent spins may in general require solving a pair of coupled differential equations[59]. However, we assume single-exponential relaxation of (j,k) spins due to the weakly coupled q-spins. From

eqs 6, 7 and 24, the following TCFs are obtained[56]:

$$G^{iDD}_{S_0S_0}(\tau) = \frac{4}{3}\sum_{q,m} I_q(I_q+1)\overline{\Delta F^{q*}_{2m}(0)\Delta F^{q}_{2m}(\tau)}, \quad (26)$$

$$G^{iDD}_{I_{j,z}I_{j,z}}(\tau) = \frac{2}{3}\sum_{q} I_q(I_q+1)g^{j,q}(\tau), \text{ with} \quad (27)$$

$$g^{j,q}(\tau) = \overline{F^{jq*}_{20}(0)F^{jq}_{20}(\tau)} + 3\overline{F^{jq*}_{21}(0)F^{jq}_{21}(\tau)} + 6\overline{F^{jq*}_{22}(0)F^{jq}_{22}(\tau)},$$

$$G^{DD}_{I_zI_z}(\tau) = \frac{3}{2}(\overline{F^{jk*}_{21}(0)F^{jk}_{21}(\tau)} + 4\overline{F^{jk*}_{22}(0)F^{jk}_{22}(\tau)}), \quad (28)$$

for singlet magnetisation (caused by the *iDD* q-spins) and intra-(j,k)-pair *DD* magnetisation relaxation, respectively: $F^{jq}_{2m}(t) = c^{DD}_{jq}\frac{D^2_{0m}[\Omega_{jq}(t)]}{r^3_{jq}(t)}$, $\Delta F^{q}_{2m}(t) = F^{jq}_{2m}(t) - F^{kq}_{2m}(t)$, and I_q is the spin quantum number of third spin. Integration of the correlation functions of eqs 26-28 into spectral densities [*cf.* eqn (4)] provides the $(T^{iDD}_S)^{-1}$, $(T^{iDD}_1)^{-1}$ and $(T^{DD}_1)^{-1}$ relaxation rates, respectively. In this work, the relaxation rates are computed in the extreme narrowing regime due to the short characteristic decay time for the TCFs. The validity of eqs 26-28 requires a fast q-spin relaxation $[(T^q_1)^{-1} \gg \{(T^j_1)^{-1},(T^k_1)^{-1}\}]$, fulfilled for the proton and quadrupole relaxation rates in the this work (typically by one order of magnitude or more), and that the characteristic molecular dynamics rotational timescale (τ_c) is short $[\tau_c^{-1} \gg \{(T^q_1)^{-1},(T^q_2)^{-1}\}]$, not to provide an additional relaxation sink[59].

6 Computational methods

Flowchart for the prediction of experimental observables from QC/MD simulation is provided in Figure 3. After preparation of an atomistic molecular MD with the explicit solvent molecules [*cf.* sec 6.1], the coordinates $\{\mathbf{r}_l(t),\mathbf{v}_l(t)\}$ of the LLS-agent and the closest solvent molecules are extracted. From $\mathbf{r}_l(t)$, the relevant information to compute both *iDD* and *DD* relaxation is available with numerical implementation of eqs 26-28. To proceed with the properties dependent on the QC computed tensors $(SR, CSA, \ldots)$, the steps 1-5 in Figure 3 are followed:

1. The spatial degrees of freedom with significant influence on the QC tensors are identified based on prior experience and tests. In this study, bond angles local to the spin pair, as well as all dihedral angles of the spin carrier molecule, are used. The coordinates of the solvent may be relevant, as well.

2. Construction of spatial-training set $\{\Theta\}$ normalized to unit interval ($\Theta^{(i)} \in [0,1]$). An efficient space filling method is adapted to the generally challenging configurational space spanned by the MD simulation. The key is to find a training set representing the complete configuration space with relatively few configurations selected from the large pool ($> 10^5$) of MD snapshots. A set $\{\Theta\}$ of typically a few hundred configurations is used. Briefly, as illustrated by insert in Figure 3, from initially selected configurations (a,b,c) an additional configuration (d) is selected based on inverse distance squared in the configuration space [*cf.* sec 6.3.1].

3. For the training set, the QC-tensors are explicitly computed. We use the DALTON[62] software for the purpose [*cf.* sec. 6.2].

4. The QC-tensors of relevance to the relaxation mechanism λ are used to parametrize a high-dimensional QCPS, employing the Kriging model[41]. The tensors for all the MD snapshots ($> 10^5$) are computed from the constructed QCPS [*cf.* sec. 6.3].

5. The spin Hamiltonians (see eqs 9,21) are assembled with the QC tensors rotated from the Eckart to the laboratory frame (sec. 4.1.1), and used to numerically compute the TCFs (sec. 5.1).

Finally, the convergence of the Kriging model is probed with respect to i) the size of the training set, by computing the observable T_S^{-1} as resulting from the mechanism λ using the whole MD trajectory and ii) the quality of the QCPS model, by explicitly computing a QC test function (here the TCF amplitude $G^{\lambda}(t_0)$ is used) using a limited set of configurations (typically 100) and evaluating the QCPS model for the same set of configurations. If the model does not converge, the training set is expanded and the steps 2-5 updated until the additional configurations no longer change the computed QCPS observable.

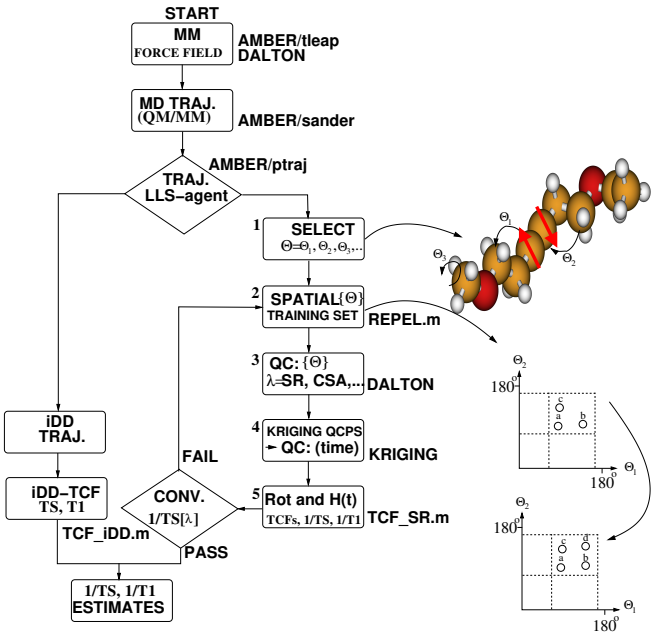

Fig. 3 Flowchart for T_1^{-1} and T_S^{-1} estimates from QM/MM trajectories and QC tensor calculations, [*cf.* sec 6]. The upper insert illustrates molecule I with a few of the considered degrees of freedom. The lower inserts illustrate the training set selection of a new configuration (d), based on the distance in the configuration space to the already existing set (a-c).

6.1 Molecular dynamics simulation

Considering the first three blocks of Figure 3, MD trajectories were computed with a quantum mechanics/molecular mechanics (QM/MM) model. This was performed with the SANDER

(MPI) module of the AMBER program package[63]. The QM region was presently chosen to consist of just the single relevant LLS candidate (see Figure 1), for which quantum-mechanically computed forces replace the force field. The dynamics is classical, with quantum treatment of forces, however. There is evidence that the QM calculation of forces improves the accuracy of the internal dynamics[64]. The QM region is modelled with the PM3 (parameter model 3) Hamiltonian, *i.e.*, a semi-empirical QM method, where typically the costly two-electron integrals are simplified with parameters adjusted to reproduce energies for a set of reference molecules[65].

MM force field. The Hamiltonian is embedded in an explicit classical solvent (MM). A single LLS-agent has been placed among the following solvent molecules in the dilute limit: **I** in 900 CH_3OH molecules, **II** in 851 CH_3OH molecules and **III** in either (dilute limit **a**) 376 DMSO-h_6 molecules, (**b**) 33 $^{15}N_2O$ in 741 DMSO-h_6 molecules and (**c**) 33 $^{15}N_2O$ in 741 DMSO-d_6 molecules, where the variants (**b**) and (**c**) correspond to about 0.5 M concentration of $^{15}N_2O$ molecules. The simulation boxes are typically of linear dimension of about 40 Å. The initial vacuum structures of the solutes were optimized with DFT B3PW91/6-31G(d,p)[62]. The solvent force field for methanol is provided in AMBER (MEOHBOX[66]) and also DMSO is available pre-parametrized[67]. The program tleap, which is included in AmberTools13, was used to generate the QM/MM parameter files. The MM (solvent) force field parameters were taken from AMBER/GAFF (General Amber Force Field) and ff99SB. The partial charges for $^{15}N_2O$ were determined using the semi-empirical QM method (AM1-SCC) implemented in the AMBER module antechamber. The QM/MM simulations were performed with periodic boundary conditions.

MD trajectory. The particle-mesh Ewald method[63] was used for the long-range electrostatic interactions, with a cutoff at 11 Å. The initial energy minimisation of the complete system consisted of 5000 steps, alternating between the steepest descent and conjugate gradient algorithms. Subsequently, equilibration was performed with a constant number of particles and normal temperature and pressure (NTP, 25°C, 1 bar) over 300 ps or more, in contact with a Langevin thermostat. The system was then equilibrated for 10 ps at constant volume (*NVT*) with a weak Berendsen thermostat (10 ps coupling constant was used). The production run consisted of a subsequent 2-8 ns *NVT* simulation with configurations stored typically every 10 fs. A 1.0 fs time step was used in the simulations. The MD simulations were done on a single 4 GB memory node (with sixteen 2.6 GHz cores on the University of Southampton supercomputer[68]). The MD simulation provided 2.8 and 3.5 ns ogf trajectory per 24 hours of simulation time for molecules **I** and **II**, respectively. Extraction of the relevant LLS-agent trajectory $\{\mathbf{r}(t),\mathbf{v}(t)\}$ was done with the program *ptraj* included in the AMBER package.

6.2 Quantum Chemistry

The focus of the present QC calculations is on the interaction tensors for the *SR* mechanism (for equilibrium configuration $\mathbf{r}^e$) and the corresponding *SIM* tensors for the training set $\{\Theta\}$ (see eqn (9) and the stage **3** of Figure 3). Both are needed to model the coupling of the nuclear magnetic moment with the intramolecular magnetic field[27].

The *SR*-tensor[69] was computed with the DALTON[62] software involving the perturbation of the ground state by the total (electronic+nuclear) and spin angular momenta. The integration over the electronic momentum and position degrees of freedom provides the interaction tensor per unit of angular momentum for the nuclear configuration Θ, as

$$\boldsymbol{C}_k^{SR}(\Theta) = [\boldsymbol{C}_k^{el}(\Theta) + \boldsymbol{C}_k^{nuc}(\Theta)]\mathbb{I}(\Theta)^{-1}, \tag{29}$$

where the components of the MCM moment of inertia $\mathbb{I}$ are given in eqn (15), and $\boldsymbol{C}_k^{el}$ and $\boldsymbol{C}_k^{nuc}$ are the tensors containing the QC-computed electronic and classical nuclear contributions, respectively. The tensor $\boldsymbol{C}_k^{el}$ is related to the nuclear shielding[69]. The relevant interaction per angular velocity (required in eqn (9)) is given by $\boldsymbol{C}_k(\Theta) = \boldsymbol{C}_k^{SR}(\Theta)\mathbb{I}(\Theta)$.

Due to the finite size of the basis set used in the calculation of magnetic properties, attention is needed to the question of gauge origin. The gauge-origin problem is addressed with rotational London atomic orbitals (LAOs) (also know as GIAOs). These orbitals are adapted with explicit dependence of rotational angular momentum and feature a good basis set convergence[69]. To maintain consistency with previous works[69,70] concerning the gauge origin, the electronic term is evaluated at MCM. Furthermore, the nonrelativistic approximation is made, as is expected to be valid[71] for the low-mass nuclei ^{13}C and ^{15}N of interest here.

6.3 Quantum chemistry property surface

The purpose of the QCPS is to replace the computationally expensive QC calculation in obtaining the Hamiltonian tensors. In this work, the QCPS is a Kriging model, a minimum mean-square error method for nonlinear spatial prediction (see Ref.[72] for a review), built from a training set of precomputed QC tensors.

The training set vector consisting of K molecular configurations is denoted as $\boldsymbol{\Theta} = [\Theta^{(1)},\Theta^{(2)},\ldots,\Theta^{(K)}]^T$, where $\Theta^{(i)}$ are the non-redundant coordinates expressed in the Z-matrix form of dimension n. These may include both intra- and intermolecular configurations and are associated with QC-computed tensor elements $C_{kl}(\Theta^{(i)})$. The format of the Kriging model is extensively discussed in the literature[41,72,73] and we provide the key aspects here. Although a completely deterministic multivariate input-to-output ($\Theta \to C_{kl}$) relation is ultimately constructed, the starting assumption takes the point-of-view that our training set of QC calculations consists of statistical observations taken from a probability distribution of $\dim(K)$ and is, thus, described by $\mathbf{C}_{kl}(\Theta) = \beta\mathbf{1} + \Sigma$. Here, β is a scalar, and $\mathbf{1}$ as well as $\boldsymbol{\Sigma}$ are the unit vector and a multivariate random variable with zero mean and covariance $\mathrm{Cov}(\boldsymbol{\Sigma}) = \sigma^2\boldsymbol{R}(\boldsymbol{\Theta},\boldsymbol{\Theta}')$, respectively. The elements of $\boldsymbol{R}$ are given by $R(\Theta^{(i)},\Theta^{(j)}) = \exp[\sum_{l=1}^{n}\rho_l|\Theta_l^{(i)} - \Theta_l^{(j)}|^2]$ and the parameters β,σ^2 and ρ_l, $(l = 1,2,\ldots,n)$ are determined by maximum likelihood estimation (MLE)[41]. This provides closed expressions for the over-

all mean and variance (for a given set $\{\rho_l\}$):

$$\beta = \frac{\mathbf{1}^T\mathbf{R}\mathbf{C}_{kl}}{\mathbf{1}^T\mathbf{R}\mathbf{1}};\ \ \sigma^2 = \frac{1}{K}(\mathbf{C}_{kl}-\mathbf{1})^T\mathbf{R}^{-1}(\mathbf{C}_{kl}-\mathbf{1}),$$

and, to estimate the set $\{\rho\}$, an iterative global optimisation algorithm by Jones *et al.*[74] was followed. The sought model output is given by

$$C_{kl}(\hat{\Theta}) = \beta + [R(\hat{\Theta},\Theta^{(1)}),\ldots,R(\hat{\Theta},\Theta^{(K)})]\boldsymbol{R}^{-1}(\mathbf{C}_{kl}-\mathbf{1}\beta) \qquad (30)$$

where the bracket $[\cdot]$ contains the correlation between the $\hat{\Theta}$, which is not in the training set, with each of the training configurations. The parameters ρ_l model the non-linear variability with respect to the spatial degree of freedom Θ_l. Note that with one of the training configurations inserted in eqn (30), the corresponding QC value is recovered, honouring the status of the training data as the best we have. Hence, the training data is explicitly included in model predictions, in addition to forming the foundation for determining the Kriging model parameters.

A simple and commonly used method to account for the uncertainty in the training data that may, for instance, originate from omitted explicit degrees of freedom in the Kriging model, besides other inaccuracies, is to work with a regression model. This may be constructed by including a *regression* parameter[41] in the Kriging model, *i.e.*, to substitute $\mathbf{\Sigma} \rightarrow \mathbf{\Sigma} + \mathbb{1}\rho_{n+1}$ (with $\mathbb{1}$ the unit matrix). Thus, the number of parameters increases by one and the overall average agreement is sought, instead of considering the training data as exact.

With one parametrized Kriging QCPS for each tensor component, the snapshots $C(\hat{\Theta}(t))$ ($\sim 10^5 - 10^6$) of the MD trajectory are computed at low cost. The largest computational cost associated with the Kriging model lies in the matrix ($\mathscr{O}(K^3)$) operations and the global optimisation of $\{\rho\}$. Provided a training set of circa 500 configurations is sufficient, a high dimensional ($\dim(\Theta)=30$) Kriging model is feasible on an ordinary workstation in the order of 10 min. The Kriging model is constructed in FORTAN77 code (see Kriging in Figure 3), implemented with blas and lapack libraries[41,75], compiled on Mac OS and Linux.

The Kriging model has been found to give more accurate results for a given training set size than the alternative surrogate models, such as radial basis-function neutral networks[44]. In addition to the quantities in eqn (30), also the model uncertainty may be estimated at a negligible additional cost[76], which opens an attractive training capability by predicting where in the configurational space any additional QC calculations are best invested. Since the QC calculations pose an overall bottleneck in the time-dependent Hamiltonian approach, the Kriging model is regarded as an attractive approach in this work and a broad range of related QC-MD problems.

6.3.1 Strategy for an efficient training set

A key to successful implementation of QCPS is a representative training set of configurations (step 2, Figure 3). Methods for a cost-effective representation of the spatial degrees of freedom exist, such as *Sobol*[41] that provides configurations in an n-dimensional unit cube. However, certain subsets of all the configurations of the current molecular model are not allowed, for instance when the atoms are in close contact. This makes *Sobol* impossible to use without an additional selection strategy to disregard physically improbable configurations. In the literature, to address the complex configuration space of MD simulations, the *Sobol* method has here been used initially, followed by iterative construction of QCPS, with subsequent removal of the unfavourable training configurations[44]. A different approach is taken in the "normal mode distortion"[77] method in which first, one computes the normal modes of the system and then generates configurations by distorting the the normal mode configuration. This comes with the system-dependent ambiguity in how much distortion can be applied for the different modes.

To enable an efficient selection including intra-, as well as intermolecular degrees of freedom, and to simplify as compared to the above-described methods, the space-filling method of Audze *et al.*[41,78] is adapted to the context of MD simulation. In the implementation, (i) a large representative pool $\{\Theta\}_{N_P}$ of all the configurations of the MD trajectory is extracted, containing N_P, typically 10^4 snapshots uniformly distributed in time, (ii) The minimum and maximum values of each $\Theta^{(i)}$ (for instance a bond angle) are determined from the MD data and the range is normalized to the interval [0,1]. Note that a QCPS is built in terms of continuous variables and, thus, the distributions of Θ are inspected to verify this. In this work we only find a few dihedral angles to be discontinuous, with population around $-\pi/2$ and $\pi/2$ (for almost a flat segment of the molecule). The distributions of these dihedral angles are easily made continuous by transforming to a $[0,\pi)$ range. Finally, (iii) after selecting the first configuration from $\{\Theta\}_{N_P}$, subsequent configurations are then based on the previously (K) selected ones by finding $\Theta^{(K+1)}$ such that the minimum

$$\min_{\Theta^{(K+1)}\in\{\Theta\}_{N_P}} \sum_{i=1}^{K}\sum_{j=i+1}^{K+1} \frac{1}{||\Delta\Theta^{(ij)}||^2}, \qquad (31)$$

is found, where $||\Delta\Theta^{(ij)}||$ is the Euclidean distance of the normalized parameters between the configurations i and j. This method finds the new configuration that is displaced the furthest (in the sense of eqn (31)) from the previously selected ones. This strategy is applicable both to small and large molecules, with or without solvent.

6.4 Setup of the MD/QC simulations

The preparation of the simulation is discussed here, bringing together the steps in Figure 3.

Force field. We note first that an independent check of the solvent dynamics is available through the diffusion constant (D) of the solvent. The solvent self-diffusion is estimated from the mean-square displacement predicted from the MD simulation (see SEI and Table S1 for complete list). Overall, the simulated results agree well with corresponding experimental values. $D(CH_3OH)$ is overestimated by only 6% in the simulation. For DMSO, both the protonated and deuterated isotopomers are simulated and the ratio $D(\text{DMSO-h}_6)/D(\text{DMSO-d}_6)$ of 1.09 is found. Thus, square-root-mass-trend seen in experiment, where the corresponding ratio is 1.14[79], is reasonably reproduced. In absolute terms, D(DMSO) is overestimated by 30% in the simulations. Given the

small effect deuterium is expected to have, we keep the protonated form of methanol in the relaxation study.

For molecules **I** and **II**, it is assumed that the dilute limit provides a relevant description for the 0.1 M experimental samples. The $^{15}N_2O$, was simulated both at the dilute limit and at about 0.5 M concentration of $^{15}N_2O$. Before considering the NMR relaxation below, we see from the radial pair correlation function for the ^{15}N(central)-^{15}N(central) distance (see Figure 4), that there is significant structure in the solvent at short distances. Typically

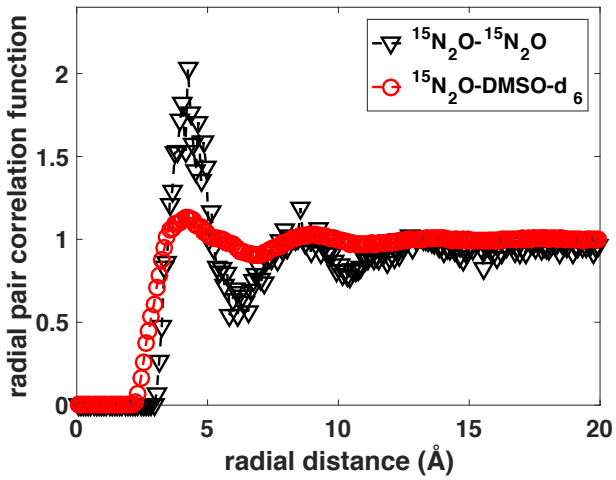

Fig. 4 Radial pair correlation functions for the solvation of $^{15}N_2O$ in DMSO: **a** ^{15}N(central)-^{15}N(central) and **b** $^{15}N_2O$-DMSO center-of-mass distance.

one neighbouring $^{15}N_2O$ is, on the average, present in the first solvation shell (at around 5 Å), even at this relatively low concentration. This motivates the relaxation study to be conducted at a finite concentration.

QC theory. In a study by Gauss *et al.*[70], the accuracy of DFT calculations for carbon and nitrogen SR-tensors is found to be reasonable, featuring only a small dependence on the particular DFT functional, as benchmarked with high-level *ab initio* QC methods, as well as compared with experiments for a large set of small molecules. In Table 1, the basis-set dependence for the Frobenius norm of the *SR* tensor is given for one MD snapshot of molecules **I**-**III**. Comparing 6-31G*, with polarisation functions on second-row atoms (denoted with *), with the larger basis sets shows a similar range of interaction, motivating this small basis set to be used. On the other hand, comparing the vacuum structure calculation with the 6-31G* basis to results obtained with implicit and explicit solvent, also displays similar values, motivating us to consider the *in vacuo* results in the construction of QCPS. Molecule **III** is found to have the computed central and terminal diagonal components (3.28, 2.41) kHz in excellent agreement with experiment[80] (3.35, 2.48) kHz. The complete tensor has one large off-diagonal element that occurs due to the product made with the inverse inertia tensor (*cf.* eqn (29)) for this almost linear snapshot. To avoid such large values, all construction of QCPS was made for the interaction tensor per unit angular velocity (see sec. 6.2).

Internal regions. A local region of atoms is required in eqn (9) (see Figure 2), from which the *SIM* angular velocity is computed. These regions are determined by testing several candidate regions, separately for each of the spins j and k, in a screening process. We are interested in the maximum contribution of $T_S[SIM]$, *i.e.*, the integral of TCF, eqn (22). For practical purposes, it is convenient not to include the tensors (needed in eqn (22)) at this stage. Instead we seek the maximum of the integrated TCF of the difference of the local angular velocities for the regions attributed to j and k, $\Delta(t) = \dot{\boldsymbol{\theta}}_j(t) - \dot{\boldsymbol{\theta}}_k(t)$. This property gives insight in the total influence of the fluctuations. In Figure 5(a), the maximum of integrated TCF of $\Delta(t)$ is sought for candidate regions attributed to j and k [scaled with the constant integrated TCF of the overall angular velocity $\boldsymbol{\omega}(t)$], for molecule **I**. The internal angular velocity $\dot{\boldsymbol{\theta}}$ is readily computed from the angular momentum and the inverse of the moment of inertia tensor, eqn (21). In Figure 5(b), the regions with maximum contribution are highlighted in red. Note that for region 13, the whole molecule, the difference the in fluctuations cancels out. A similar study for molecule **II** is illustrated in Figure 6, showing the largest amplitude from the three-atom region for both spins j and k (displayed in red, in panel b).

The same type of exploration was performed for molecule **III**, as displayed in Figures S1 and S2 of SEI. Several combinations of internal regions give almost the same magnitude of fluctuations and also give approximately the same T_S^{-1} relaxation rate. The largest fluctuations are found for the single oxygen as the internal region for the central nitrogen and both nitrogens as the internal region for the terminal ^{15}N spin. Note that an internal group consisting of a single atom (oxygen in this case) has only two axes of rotation and the inverse moment of inertia tensor is computed from the associated two eigenvalues. The two nitrogens (for a bent $^{15}N_2O$), have formally three axes of rotation and the internal angular velocity may be computed accounting for all these. This gives the mean T_1^{-1}, T_S^{-1} estimates consistent with the study described below. The statistical variability in the estimates is very large, however. It is expected that a roundoff error in $\dot{\boldsymbol{\theta}}_k(t)$ may occur for nitrogens almost aligned with the MCM, where one very large component of the inverse moment of inertia tensor is compensated by the corresponding angular momentum component, which almost equals zero (see eqn (21)). To avoid this problem, both internal regions for $^{15}N_2O$ are assumed to have only two axes of rotation.

A suitable time step in the integral of TCFs, after exploring the range of 2.5-20 fs, is 5 fs for the molecules **I** and **III**, and 10 fs for the molecule **II**. This defines the resolution at which the MD snapshots are saved. Note that a too long time step may have a large impact on these integrals, as well as for the forthcoming spectral densities.

Remote internal regions. A simplified estimate for the remote internal regions is discussed in this section. To proceed, consider the nuclear contribution to the *SIM* tensor

$$\boldsymbol{C}_k^{nuc} = \alpha^2 \gamma_k \sum_l \frac{Z_l}{r_{lk}^3} [(\mathbf{r}_{lk} \cdot \mathbf{r}_{lk}) \mathbb{1} - \mathbf{r}_{lk} \mathbf{r}_{lk}], \qquad (32)$$

where α is the fine structure constant, γ_k the gyromagnetic ra-

Table 1 Basis-set dependence of the Frobenius norm[a] of the *SR* tensors (kHz) calculated at the DFT/B3PW9 level, for one MD snapshot for molecules **I**-**III**. ^{13}C Nuclei j and k are depicted for molecules **I** and **II** in Figures 5 and 6, respectively. For molecule **III**, t denotes terminal and c the central ^{15}N nucleus. The diagonal component is listed in brackets for the molecule **III**.

	molecule **I**		molecule **II**		molecule **III**	
Basis	$\|\|C_j^{SR}\|\|$	$\|\|C_k^{SR}\|\|$	$\|\|C_j^{SR}\|\|$	$\|\|C_k^{SR}\|\|$	$\|\|C_c^{SR}\|\|$	$\|\|C_t^{SR}\|\|$
6-31G*	0.2894	0.2859	0.2578	0.2833	76.70 (3.289)	203.16 (2.261)
(6-31G*)[b]	0.2660	0.2459	0.2557	0.2892	-	-
(6-31G*)[c]	0.3049	0.2495	-	-	-	-
6-311G*	0.2926	0.2919	0.2825	0.3126	86.46 (3.610)	232.62 (2.531)
cc-pVDZ	0.2946	0.2951	0.2608	0.2867	208.16 (3.359)	208.16 (2.333)
aug-cc-pVDZ	0.3211	0.3211	0.2637	0.2915	77.72 (3.370)	210.07 (2.340)

[a] $||C^{SR}|| = \sqrt{\sum_{l,m}|c_{lm}|^2}$.

[b] Polarizable continuum model with the methanol dielectric constant.

[c] Solute and eight explicit solvent molecules.

tio, Z_l the charge of nuclei l and $\mathbf{r}_{lk}$ is the vector pointing from the lth to the kth nucleus. Note that the nuclear (as well as the electronic) contribution is dependent on the gyromagnetic ratio. Hence, the relaxation rate depends on γ_k^2. When nuclear dynamics is described with classical mechanics for a remote group of atoms, using $\boldsymbol{C}_k^{nuc}$ contribution only, a $1/r^3$-dependent dipole field[27] results (*i.e.*, a factor $1/r$ arises from eqn (32) and $1/r^2$ from $\mathbb{I}^{-1}$). To model the remote regions, the classical Biot-Savart law description is considered. The molecule **I** is found to be highly flexible and to have the largest influence of the remote regions, as compared to the molecule **II**, the naphtalene derivative studied in Ref.[15], and several other medium-sized molecules (not studied in this work). All remote, flexible regions are included, *i.e.*, CH_3, CH_2, CD_2, and C−O−C, a total of 7 groups for molecule **I**. The time-dependent interaction tensors are available from eqn (32) by replacing the absolute nuclear charges with their partial atomic charge counterparts, obtained from Mulliken population analysis of the electronic wave function. The contributions to T_S^{-1} from all the remote *SIM* regions are added up. The dynamics of the the remote fluctuating regions is accurately accounted for and, thus, reflect their distance dependence. In spite of the large number of regions included, the contribution of remote internal regions to T_S is longer than about one month or, for T_S^{-1}, three orders of magnitude less than the local-region *SIM* rates presented for molecule **I** below. However, in this test where partial charges are applied, the electronic contribution is not explicitly included. To estimate the error arising from the classical description, the same local regions used in the fully explicit method described below, were also computed. The comparison show that the classical approximation underestimates the contribution to the relaxation rate by a factor of no less than 13. To summarize, the classical description for the remote regions would nevertheless have a negligible contribution even if we made an (approximate) calibration using the full theory. This motivates the following study to be performed with only the local regions residing in close proximity of the spins. The small influence of the remote regions can be expected from the $1/r^6$ distance dependence of the contributions to the relaxation rate.

Numerical estimation of spectral densities. In practice, the spin Hamiltonian trajectory is divided into L time-blocks of length equal to three times the rotational correlation time, or more. These blocks are essentially uncorrelated and, from the stationarity (equilibrium) property of MD simulations, L separate estimates of the observables are calculated. Thus, a correlation function at time step n for the stochastic process $\boldsymbol{B}(t)$ is computed as $G(\tau_n) = 1/L\sum_{m=1}^{L}\{G(\tau_n)\}_m$, where $\{G(\tau_n)\}_m$ contains the statistical information that can be extracted from the single trajectory block m. To make the most of each block, the TCF needs to be computed as the "sum-over time origins"

$$\{G(\tau_n)\}_m = \frac{1}{O_n}\sum_{t_0}^{O_n}\{\boldsymbol{B}^\dagger(t_0)\cdot\boldsymbol{B}(t_0+\tau_n)\}, \qquad (33)$$

where O_n is the number of time origins (t_0) that are choosen for the TCF at time step n. The statistical information content is thus greater in the initial section of TCF.

With the assumption that $\{G(\tau_n)\}_m$ is a Gaussian random variable, the statistical error may be estimated as $t_{\alpha,L-1}\sqrt{var[\{G(\tau_n)\}_m]/L}$, where $var[\cdot]$ denotes the estimated variance and t the t-distribution for statistical significance. The Gaussian assumption is motivated by the central limit theorem[81]. The value of the coefficient t is kept at unity and L equal to 10, corresponding to 70% and 85% two- and one-sided confidence intervals, respectively[81]. Statistical errors for the relaxation rates (T_1^{-1}, T_S^{-1}) are computed similarly.

The spectral densities are obtained by integrating the TCFs for each block and and taking the mean over the L blocks. Consistent evaluations of the *SIM* and *SR* integrals are obtained by extracting the limiting values after typically one reorientational correlation time, as exemplified by the inserts [*cf.* Figures 10 and 11], showing the cumulative integrals (by the trapezoidal method[82]). This is even though the majority of *SIM* and *SR* TCFs decay at a much shorter (collision-modulated) timescale. The dipole-dipole spectral densities are computed from the sum of two exponentials fitted to the weighted TCF [*cf.* eqs 26-28].

Convergence of the QCPS. The first step in setting up the QCPS is to decide on the relevant degrees of freedom, where a

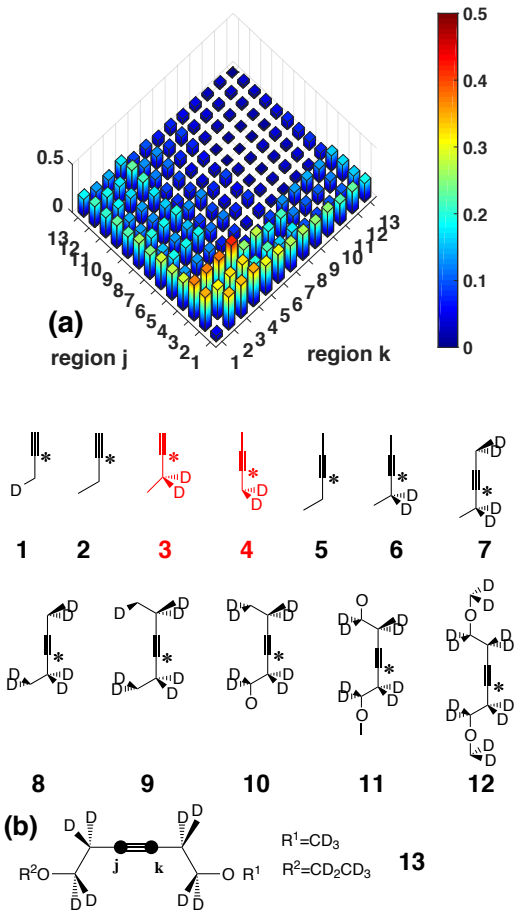

Fig. 5 Panel (a): Ratio of the integrated TCF $(\langle\Delta^2\rangle\tau_\Delta)/(\langle\omega^2\rangle\tau_\omega)$ of the difference in the j,k-internal region angular velocities $[\Delta(t)=\hat{\boldsymbol{\theta}}_j(t)-\hat{\boldsymbol{\theta}}_k(t)]$ and the overall molecular angular velocity $\omega(t)$. The τ_x $(x=\Delta,\omega)$ denotes the integral of the corresponding TCF, normalized to unity. Panel (b): The thirteen explored candidates for the internal regions of molecule **I**, with the regions for just *one* spin (denoted with *) shown. The corresponding region for the other spin is given by inversion with respect to the triple bond, the point of local inversion symmetry.

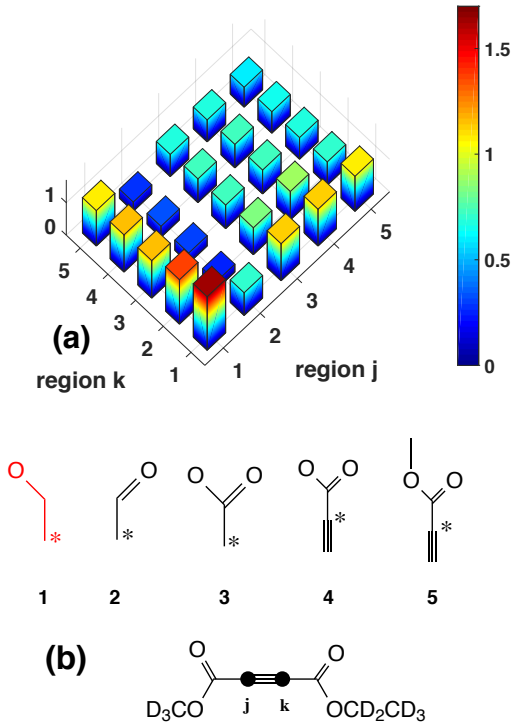

Fig. 6 Explored internal regions for molecule **II**, see Figure 5 for details.

balance must be found between the computational cost implied by the dimensionality and impact of the approximations on the computed observable. Self-evidently, the conformational changes local to the spin pair are expected to have a direct influence on the interaction tensors and, therefore, the initial constructed model only had five degrees of freedom: the *j*-*k* bond length, as well as the local dihedral and bond angles, for the molecule **I**. This model was complemented with an 18-dimensional model including all the local dihedral and bond angles, the *j*-*k* bond length, as well as all the dihedral angles throughout the molecule **I** (omitting hydrogen centers). Adapting the latter model reduced $T_S^{-1}[SIM]$ by a factor of two, suggesting that the overall molecular conformation may have an explicit influence on the interaction tensors. The latter strategy was then followed for molecules **I** and **II**, leading to 18- and 21-dimensional models in these cases, respectively. The tensors are expressed as sums of zero-, first- and second-rank parts and a distinct QCPS is constructed for each part, since different physical processes may be important for these components.

The degrees of freedom not explicitly included in the QCPS model are still present in the training set of QC calculations and, thus, their average contribution is implicitly included. The three internal degrees of freedom for molecule **III** were included in the QCPS, also in this case excluding the solvent.

The second step is to establish a converged QCPS Kriging model. In particular, two questions are considered: (i) what is the sufficient size of the training set and (ii), what is the absolute error based on the above-chosen explicit degrees of freedom? To address question (i), the relevant observable is computed according to the following recipe: (1) construction of time-dependent tensor (eqn (30)) for various training set sizes K up to K_{max}, obtained by the method of eqn (31); (2) obtaining the internal and overall angular velocity (eqn (21)), where the latter is computed for a rigid reference structure of the molecule; (3) integrating TCFs (eqn (23)), with the $SIM+SR$ contribution to study $T_S^{-1}[K]/T_S^{-1}[K_{max}]$. The aspect (ii) needs to be addressed separately since we need to discriminate between several QCPS models. From a batch of 100 configurations not included in the training set, the TCF value $\tilde{G}(t_0)$ is computed by explicit QC as well as using two QCPS models. The deviations are computed as shown in Figures 7 and 8 for molecules **I** and **II**, respectively. Both the interpolation and regression Kriging models were explored. A regression model may be motivated for these training sets where the deuterium degrees-of-freedom are not explicitly included in the model and, hence, play the role of "noise". From panels **a** and **b** in Figure 7, the singlet state (blue circles) is well-described ($dev < 10\%$) and magnetization (red triangles) is un-

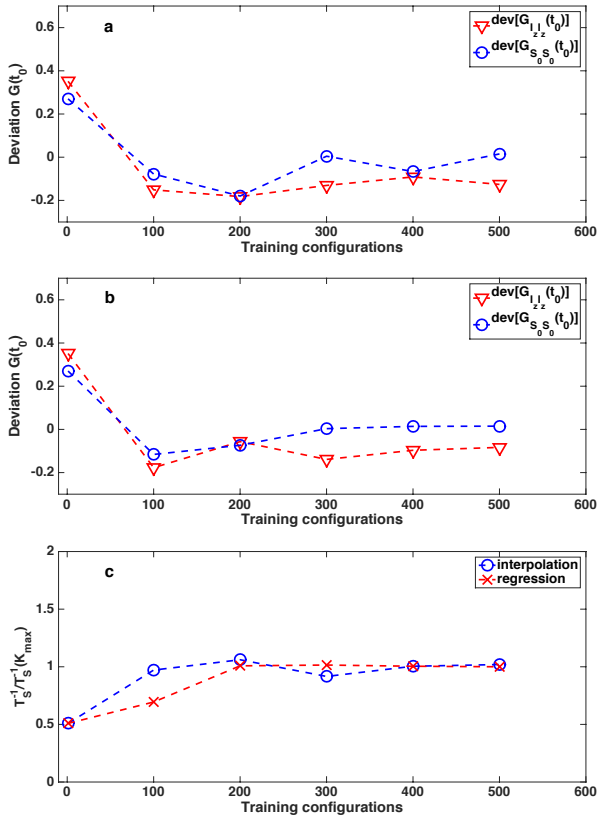

Fig. 7 (**a**,**b**) Deviation of the initial amplitude of $SIM + SR$ TCF ($dev[G(t_0)] = [\tilde{G}(t_0) - G(t_0)]/\tilde{G}(t_0)$) for molecule **I**, obtained from the direct QC-computed tensors $\tilde{G}(t_0)$ as well as with the surrogate model $G(t_0)$, for a batch of 100 configurations not included in the training set in the interpolation and regression models in panels **a** and **b**, respectively. Panel **c** shows the ratio of T_S^{-1} and $T_S^{-1}(K_{max})$ where the latter is computed with K_{max} =500 training configurations and interpolation scheme.

derestimated ($dev \sim 10\%$) for both models. Panel **c** suggests that the regression model converges with slightly fewer (about 300) training configurations. However, at the converged limit, approximately the same results are obtained. The situation is similar for molecule **II** (see Figure 8**a-b**), where the singlet state is the better-modelled property, the magnetization amplitude is overestimated by about 10% and convergence is seen after 400 training configurations (panel **c**). Note that the case of $K = 1$ which denotes the single equilibrium frame, is independent of the QCPS model and deviates by a factor of 4.5 from the converged QCPS model result, in Figure 8**c**. Since ensemble properties are considered in the test, this is a convergence in distribution[81] (also denoted weak convergence). This means that we cannot benefit from the conventional arsenal of convergence tests used in machine learning[41], where explicit agreement is sought, rather than an accurate ensemble average. In this work we have carried out additional QC calculations to obtain an independent test. However, it is expected that, by testing the QCPS model toward the relevant observable, fewer training data are required. Note that the *SR* tensors are computed for the rigid-molecule angular velocity and static tensor (see sec. 5.1), hence the influence of the conformational change of the QCPS is isolated to the *SIM* Hamiltonian. The same convergence test for $^{15}N_2O$ shows only a minor variation of circa 1% with the training-set size in the range between 100 to 200 molecular configurations.

The QCPS model used here is restricted in dimensionality, an increase in which requires a significantly larger training set and may cause numerical challenges in the Kriging parameterization. Computing with explicit solvent would cause such a drastic increase in the dimensionality. The effect of solvent may be included at negligible extra cost in an implicit form. Alternatively, an average influence of the solvent, thus including solvent in the training configurations, but not increasing the model dimensionality, may be a route forward. However, these two solvent representations omit some of the dynamics and may lead to false conclusions concerning relaxation. In this work we test the hypothesis of only including intramolecular degrees of freedom in the QCPS, thus omitting solvent. The result in Table 1 suggest that the solvent does at least not give rise to order-of-magnitude differences, justifying this approach for theses systems. It is left for forthcoming work to systematically address higher-dimensional QCPS models, where explicit solvent influence may be included.

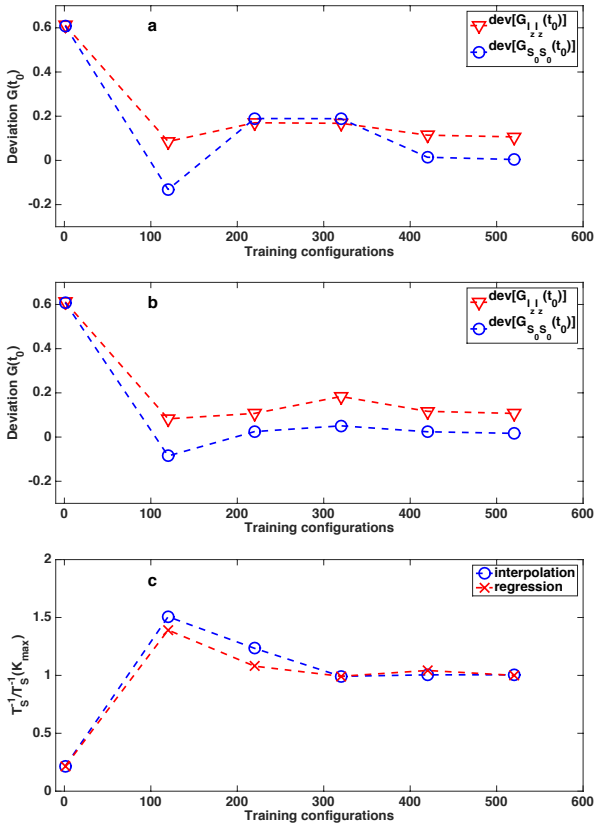

Fig. 8 Deviation in surrogate model for molecule **II** explored up to 520 training configurations, see Figure 7 for details.

7 Results and discussion

We explore the MD-QC model estimates for the mechanisms *iDD*, *SIM*, *SR* and the interference therm $SIM \times SR$. This information and the total T_S and T_1 contributions, together with the experimental decay times at 2.2 mT are listed in Table 2. These results

Table 2 Experimental and simulated longitudinal (T_1) and singlet (T_S) relaxation times (EXP and Cal), as well as the individual relaxation rate contributions.

	T_1 (s)		$1/T_1 \times 10^{-3}$ (s^{-1})				
MOL	EXP	Cal	*DD*	*iDD*	*SIM*	*SR*	$SIM \times SR$
I	51.5±0.8	62±8	12±1	0.3, 0.1[a]	2.6±0.15	0.9±0.04	∼0
II	42±0.5	52±15	18±3	0.06	0.4±0.1	0.55±0.02	0.3
III[b]	-	436±50	0.36	-	∼0	1.9±0.26	∼0
III[c]	197±5	340±52	0.21	-	0.9±0.4	2.7±0.5	-0.9±0.4
	T_S (min)		$1/T_S \times 10^{-4}$ (s^{-1})				
I	10.2±1	14.4±3	-	2.6±0.6, 0.2±0.01[a]	8.7±1.3	0.09	∼0
II	15.9±0.3	13±8	-	0.3±0.05	11.0±4	0.27±0.01	1.3±0.4
III[b]	-	75±14	-	-	0.6±0.3	1.6±0.4	∼0
III[c]	26±1	18.2±6.8	-	-	8.7±3	3.0±1	-2.6

[a]) Contributions from deuterium and proton spins are given, in this order.
[b]) Simulation: 0.5M N_2O and protonated solvent.
[c]) Simulation: 0.5M N_2O and deuterated solvent.

are discussed below for each molecule.

Molecule I: The dominating magnetization relaxation mechanism is provided by the *j-k DD* interaction, followed by the *SIM* term with one-fifth contribution to the total relaxation rate. These two mechanisms explain the experimental recording at $T_1 = 51$ s, overestimatimated by 20%. The intramolecular iDD terms have only a minor contribution dominated by the deuterium spins in close proximity, over the contributions from the protons. For the singlet-state relaxation, the *DD* mechanism no longer dominates, first and foremost due to the lack of an in-pair mechanism. Secondly, not only is the amplitude of the relevant *iDD* TCF smaller (eqn (26)), but also the decay is faster by a factor of three, as is seen in Figure 9(**I**).

Highlighting the $T_S^{-1}[iDD]$ modelling options, we have first the assumption of a *rigid* molecule conformation and a single exponential TCF[17,19,20,83]. A characteristic correlation time for this hypothesis may in a realistic way be extracted from MD simulation from the TCF for molecules **I** and **II** from the TCF of the *j-k* vector, where intramolecular dynamics only have a minor influence. This result is quantitatively different (concerning the the characteristic correlation time by a factor of three) to the second option where all the explicit internal dynamics of $G^{iDD}_{S_0S_0}(\tau)$ is accounted for, as illustrated in Figure 9(**I**,**II**, solid-red). Hence, this motivates the use of MD simulations, not only to avoid explicit adjustable parameters, but also not to overestimate $T_S^{-1}[iDD]$, as may be done following the rigid molecule structure hypothesis. For the same reason, the simulated result suggests caution in extracting reorientation correlation time from T_1 experiments and using this to model $T_S[iDD]$ [19,83].

For the singlet state, the dominating mechanism is *SIM*. This mechanism is computed using the angular velocity from the internal regions, shown in Figure 5. The TCF for the total $SIM+SR$ interaction is given in Figure 10(**I**), displaying a fast oscillatory behavior, expected to originate from the torsional and slower vibrational modes within the molecule. The sum of the *SIM* and *iDD* relaxation mechanisms ($T_S \sim 14$ min) is sufficient to explain the experimentally recorded value (10 min).

Molecule II: The magnetization relaxation is explained by the

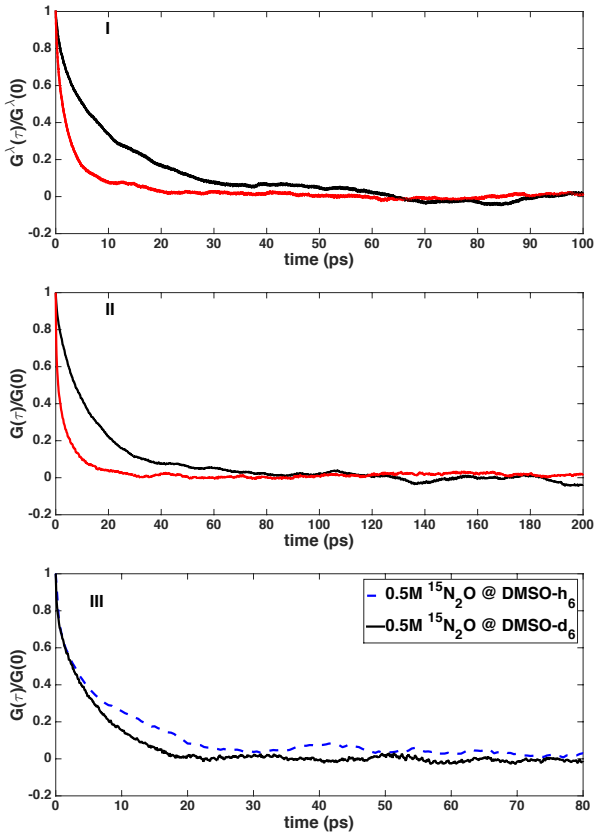

Fig. 9 TCFs for the DD mechanism: $G^{DD}_{I_zI_z}(\tau)/G^{DD}_{I_zI_z}(0)$ (^{13}C-^{13}C, solid, black), $G^{iDD}_{S_0S_0}(\tau)/G^{iDD}_{S_0S_0}(0)$ (^{2}H-^{13}C, solid, red), for molecules **I** and **II**. TCFs for the molecule **III** display $G^{DD}_{I_zI_z}(\tau)/G^{DD}_{I_zI_z}(0)$ for the protonated (dashed line) and deuterated (solid line) solvents.

in-pair DD mechanism, with a negligible contribution from *iDD*, *SR* and *SIM* terms, the experimental $T_1 = 42$ s is with the simulation result overestimated by 24%, at 62 s. The small *iDD* contribution may be understood to result from deuterium at a long distance from the spin pair (see Figure 1). Also for this molecule, the *iDD* singlet relaxation TCF decays faster than the *j-k* vector by a factor of four [see Figure 9(**II**)], again revealing that important intramolecular dynamics is accounted for. The experimental singlet relaxation time, $T_S = 16$ min, is reproduced by the *SIM* relaxation mechanism, with the total computed result underestimated at 13 ± 8 min.

Molecule III: The first simulation was done at the dilute limit with a single $^{15}N_2O$ molecule in DMSO-h_6. However, this system displays an unexpectedly small singlet relaxation rate, with T_S at about 9 hours. Finite $^{15}N_2O$ concentration (at approximately 0.5 M) was simulated in both DMSO-h_6 and DMSO-d_6, to explore the clustering and the solvent isotope (mass) effect. In this format, the $^{15}N_2O$ solution displays structure at short distances (Figure 4), meaning that we need to consider the solvent in the relaxation study.

For $^{15}N_2O$, the DD TCF actually decays faster in the DMSO-d_6 environment (with higher viscosity) than in DMSO-h_6, with the integrated correlation time shorter by a factor 0.6 [see Figure 9(**III**)]. T_1 is dominated by the *SR* relaxation mechanism, with the experimental value at 197 s overestimated by 70%, and resulting in 340 s in DMSO-d_6. The computed T_1 values for the central and terminal ^{15}N nuclei, 251±50 s and 523±100 s respectively, have the ratio of 0.47. Adding the computed estimate for $T_1^{-1}[CSA]$ at 7.04 T (see ESI), the ratio becomes 0.50, in reasonable agreement with the ratio of 0.58 recorded in the experiment[28]. The singlet state displays a large sensitivity to the small isotopic mass change of the solvent, changing T_S by a factor of four. The experimental datum at $T_S = 26$ min, is slightly underestimated with 18 ± 6.8 min as simulated for the deuterated solvent and dominated by the *SIM* mechanism. This is contrary to previous works where either the dominating mechanisms are suggested but not concluded[29] (in DMSO-d_6 solvent) or *SR* is proposed to be the dominating mechanism[21] (in H_2O, CS_2 and isopropanol), based on Hubbard model[25].

The normalized TCF $G^{SR,SIM}_{S_0S_0}(\tau)$, provided in Figure 10(**III**), displays a rapid oscillation at the frequency of circa 516 cm^{-1}. This oscillation is consistent with the NNO bending frequency. This frequency is present, although with a lower amplitude, also in the $G^{SR,SIM}_{I_zI_z}(\tau)$ TCF [Figure 11 panel (**III**)].

It is difficult to *a priori* argue, based on basic system properties, when the *SIM* relaxation process is important, or to predict its temperature dependence, as already noted for the spin-internal rotation[31,33] mechanism. Based on the *SIM* TCFs that contain molecular oscillations, the relaxation rates depend on how these motional modes are dissipated into the molecular rotational and solvent dynamics which determine the TCF decay rate and the TCF amplitude, related to the kinetic energy of the *SIM* regions. Hubbard's model in the diffusion limit[25,33] cannot be expected to be generally valid for *SIM*, pointing towards the conclusion that detailed simulations are needed also to conclude on the temperature trends. A *posteriori*, the greater $T_1^{-1}[SIM]$ influence on

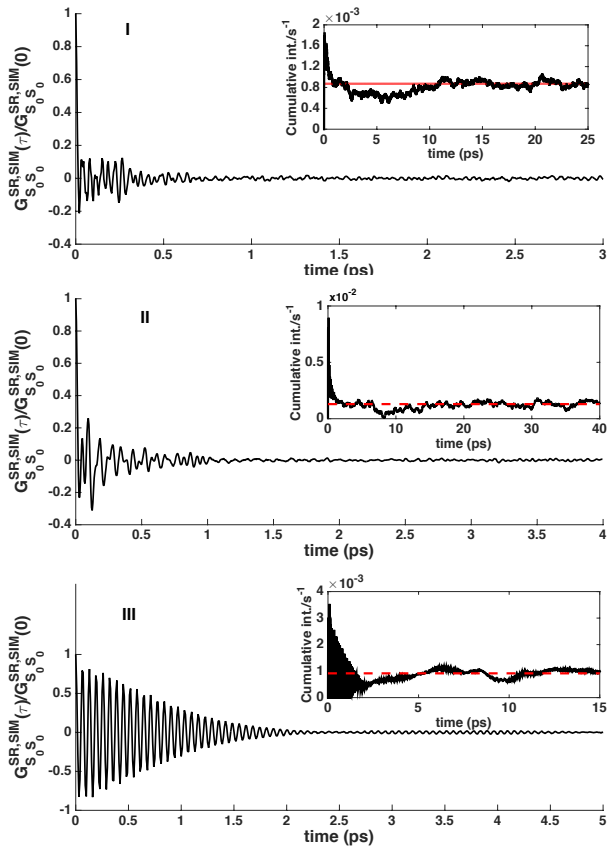

Fig. 10 TCFs for singlet relaxation [$G^{SR,SIM}_{S_0S_0}(\tau)$] computed from from MD trajectories. Panels **I**-**III** refer to the molecular systems depicted in Figure 1. The inserts show the cumulative integrals of the TCFs, providing extreme narrowing estimates of $T_S^{-1}[SR,SIM]$. The estimated relaxation rate is indicated with red dashed line, the limit value of the integral (after typically one reorientation correlation time).

molecule **I** as compared to molecule **II** (see Table 2) may, since the interaction tensors are similar in magnitude, be understood to arise from the greater flexibility and kinetic energy of the *SIM* regions of molecule **I**, which increases the amplitude. For the singlet state, the observation is that the TCF decays slower for **II** [see Figure 10(**I**, **II**)], and the larger $T_S^{-1}[SIM]$ has a more complex explanation, since the correlation between two local fields is considered (*cf.* eq 22).

Related to the viscosity and temperature dependence of $T_1^{-1}[SR]$ for molecule **III**, we note (see Table 2) the trend expected from the Hubbard model, that the *SR* contribution is inversely proportional to the reorientational correlation time[25]. However, for this system, the macroscopic viscosity of DMSO does *not* provide means to estimate the reorientational time by Stokes-Einstein relation[21], due to the complex solvent structure, thus motivating carrying out the MD simulation also in this case.

8 Conclusion

A long-lived nuclear spin state, for instance in combination with spin hyperpolarization[13,14], allows for slow molecular processes to be measured as well as opens possibilities for new MRI applications and hence, is important for magnetic resonance method de-

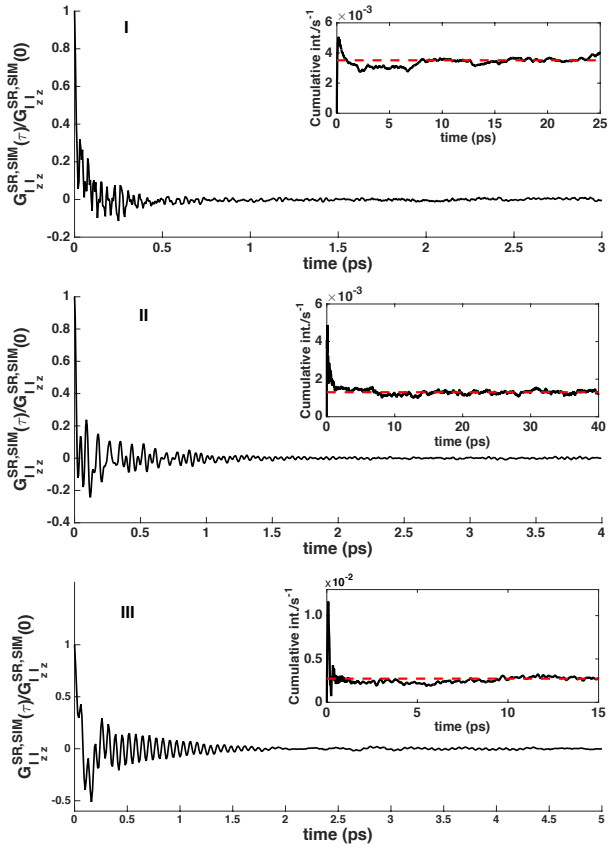

Fig. 11 TCFs for longitudinal relaxation, $G^{SIM,SR}_{I_zI_z}(\tau)$, computed from MD trajectories. Panels I-III refer to the molecular systems depicted in Figure 1. The inserts show the cumulative integrals of the TCFs, providing extreme narrowing estimates of $T_1^{-1}[SR,SIM]$. The estimated relaxation rate is indicated with red dashed line, the limiting value of the integral (after typically one reorientational correlation time).

velopment. The possibility to compare LLS-candidates with simulations, in part based on the low-field methodology detailed in this work, has opened for the design of LLS molecules[15,16].

We present a general methodology to compute time-dependent spin Hamiltonian trajectories, as well as the singlet-order and magnetization relaxation rates for the *SR*, *SIM* (spin-internal motion) and *DD* mechanisms, without adjustable parameters.

The steps required are (1) MD-simulation, (2) construction of an interaction-tensor property surface, (3) selection of the *SIM* regions, (4) assembly of the Hamiltonian, and (5) computation of the spectral densities. A key feature is the Kriging interpolation approach, which enables constructing a QCPS, as well as time-dependent QC tensors with a detailed account for a large sub-set of the degrees-of-freedom of the system, still avoiding prohibitively large QC calculations. Here, a space-filling construction of the initial training data is provided, which is found essential for the efficient and general application of the Kriging model to MD trajectories.

A key to the development of nuclear singlet-state relaxation is to fill the knowledge gap in understanding the low-field relaxation mechanisms. This work shows that *SIM* is a mechanism that needs to be considered, in order for the simulation methodology to provide a reasonably quantitative agreement with experiment.

The time-dependent QCPS tensors give greater singlet relaxation rates by up to a factor of 4.5, as compared to the static equilibrium tensors, hence the time dependence of the tensors is essential. The work highlights a potential oversimplification in applying the rigid-molecule assumption[17,19,21,83] to the singlet-state relaxation from intramolecular dipole-dipole interaction.

Additional mechanisms arising, *e.g.*, from any residual paramagnetic compounds, as well as refined tensor calculations by considering explicit solvent, are clearly of interest. Such developments may be needed for detailed temperature-dependent studies as well as more complex systems, and are left for future work. The QCPS methodology sets up a framework to compute additional singlet-state relaxation mechanisms. Work along these lines is currently in progress.

Acknowledgement

The author is grateful for very valuable discussions with and suggestions from Prof. Malcolm Levitt, Dr. Giuseppe Pileio and Dr. Gabriele Stevanato (University of Southampton), as well as from Prof. Juha Vaara, Jyrki Rantaharju, and Dr. Perttu Lantto (University of Oulu). The author acknowledge funding from 291044-HYPERSINGLET grant from the European Research Council and the EU Horizon 2020 research and innovation programme under the Marie Sklodowska-Curie grant No 703446. The author is grateful for the Kriging software supplied by Prof. Prasanth B. Nair (University of Toronto).

References

1 M. Carravetta, O. Johannessen and M. H. Levitt, *Phys. Rev. Lett.*, 2004, **92**, 153003.
2 M. Carravetta and M. H. Levitt, *J. Am. Chem. Soc.*, 2004, **126**, 6228–6229.
3 M. H. Levitt, *Encycl. Nucl. Magn. Reson.*, Wiley, Chichester, UK, 2010, pp. 1–73.
4 Y. Feng, R. M. Davis and W. S. Warren, *Nat. Phys.*, 2012, **8**, 831–837.
5 Y. Feng, T. Theis, T.-L. Wu, K. Claytor and W. S. Warren, *J. Chem. Phys.*, 2014, **141**, 134307.
6 Y. Zhang, P. C. Soon, A. Jerschow and J. W. Canary, *Angew. Chem. (Int. ed.)*, 2014, **53**, 3396–9.
7 G. Stevanato, S. Singha Roy, J. Hill-Cousins, I. Kuprov, L. J. Brown, R. C. D. Brown, G. Pileio and M. H. Levitt, *Phys. Chem. Chem. Phys.*, 2015, **17**, 5913–5922.
8 G. Pileio, M. Carravetta and M. H. Levitt, *Proc. Natl. Acad. Sci. USA*, 2010, **107**, 17135–9.
9 M. C. D. Tayler and M. H. Levitt, *Phys. Chem. Chem. Phys.*, 2011, **13**, 5556–5560.
10 S. J. Devience, R. L. Walsworth and M. S. Rosen, *Phys. Rev. Lett.*, 2013, **111**, 5.
11 T. Theis, Y. Feng, T. Wu and W. Warren, *J. Chem. Phys.*, 2014, **140**, 014201.
12 G. Pileio, J.-N. Dumez, I.-A. Pop, J. T. Hill-Cousins and R. C. D. Brown, *J. Magn. Reson.*, 2015, **252**, 130–134.
13 P. R. Vasos, A. Comment, R. Sarkar, P. Ahuja, S. Jannin,

J.-P. Ansermet, J. A. Konter, P. Hautle, B. van den Brandt and G. Bodenhausen, *Proc. Natl. Acad. Sci. USA*, 2009, **106**, 18469–73.
14 G. Pileio, S. Bowen, C. Laustsen, M. C. D. Tayler, J. T. Hill-Cousins, L. J. Brown, R. C. D. Brown, J. H. Ardenkjær-Larsen and M. H. Levitt, *J. Am. Chem. Soc.*, 2013, **135**, 5084–5088.
15 G. Stevanato, J. T. Hill-Cousins, P. Håkansson, S. S. Roy, L. J. Brown, R. C. D. Brown, G. Pileio and M. H. Levitt, *Angew. Chem. (Int. ed.)*, 2015, **54**, 3740–3743.
16 J. T. Hill-Cousins, I.-A. Pop, G. Pileio, G. Stevanato, P. Håkansson, S. S. Roy, M. H. Levitt, L. J. Brown and R. C. D. Brown, *Org. Lett.*, 2015, **17**, 2150–2153.
17 A. K. Grant and E. Vinogradov, *J. Magn. Reson.*, 2008, **193**, 177–90.
18 E. Vinogradov and A. K. Grant, *J. Magn. Reson.*, 2007, **188**, 176–182.
19 G. Pileio, J. T. Hill-Cousins, S. Mitchell, I. Kuprov, L. J. Brown, R. C. D. Brown and M. H. Levitt, *J. Am. Chem. Soc.*, 2012, **134**, 17494–17497.
20 M. C. D. Tayler, S. Marie, A. Ganesan and M. H. Levitt, *J. Am. Chem. Soc.*, 2010, **132**, 8225–7.
21 R. K. Ghosh, S. J. Kadlecek, N. N. Kuzma and R. R. Rizi, *J. Chem. Phys.*, 2012, **136**, 174508.
22 Y. Zhang, K. Basu, J. W. Canary and A. Jerschow, *Phys. Chem. Chem. Phys.*, 2015, **17**, 24370–24375.
23 C. S. Johnson, Jr. and J. S. Waugh, *J. Chem. Phys.*, 1961, **35**, 2020–2024.
24 G. Flynn and J. D. Baldeschwieler, *J. Chem. Phys.*, 1962, **37**, 2907–2918.
25 P. S. Hubbard, *Phys. Rev.*, 1963, **131**, 1155–1165.
26 A. Laaksonen and R. E. Wasylishen, *J. Am. Chem. Soc.*, 1995, **117**, 392–400.
27 W. H. Flygare, *Chem. Rev.*, 1974, **74**, 653–687.
28 G. Pileio, M. Carravetta, E. Hughes and M. H. Levitt, *J. Am. Chem. Soc.*, 2008, **130**, 12582–3.
29 J. Bocan, G. Pileio and M. H. Levitt, *Phys. Chem. Chem. Phys.*, 2012, **14**, 16032–40.
30 A. S. Dubin and S. I. Chan, *J. Chem. Phys.*, 1967, **46**, 4533.
31 T. E. Bull, *J. Chem. Phys.*, 1976, **65**, 4802–4815.
32 J. W. Lee, *J. Korean Chem. Soc.*, 1976, **20**, 364–373.
33 J. W. Lee, *Bull. Korean Chem. Soc.*, 1983, **4**, 48–54.
34 D. S. Chung, E. M. Kim and K. J. Shin, *Chem. Phys. Lett.*, 1984, **108**, 283–287.
35 M. Odelius, C. Ribbing and J. Kowalewski, *J. Chem. Phys.*, 1995, **103**, 1800.
36 M. Hanni, P. Lantto and J. Vaara, *Phys. Chem. Chem. Phys.*, 2011, **13**, 13704–8.
37 J. Rantaharju, J. Mareš and J. Vaara, *J. Chem. Phys.*, 2014, **141**, 014109.
38 J. Mareš, M. Hanni, P. Lantto, J. Lounila and J. Vaara, *Phys. Chem. Chem. Phys.*, 2014, **16**, 6916–24.
39 J. Schmidt, J. Hutter, H.-W. Spiess and D. Sebastiani, *ChemPhysChem*, 2008, **9**, 2313–2316.
40 J. Rantaharju and J. Vaara, *Phys. Rev. A*, 2016, **94**, 043413.
41 A. J. Keane and P. B. Nair, *Computational Approaches for Aerospace Design The Pursuit of Excellence*, John Wiley & Sons Ltd, West Sussex PO19 8SQ, 2005.
42 J. Sacks, W. J. Welch, T. J. Mitchell and H. P. Wynn, *Stat. Sci.*, 1989, **4**, 409–435.
43 J. P. Kleijnen, *Eur. J. Oper. Res.*, 2009, **192**, 707–716.
44 C. M. Handley, G. I. Hawe, D. B. Kell and P. L. A. Popelier, *Phys. Chem. Chem. Phys.*, 2009, **11**, 6365–6376.
45 P. Håkansson, T. Nguyen, P. B. Nair, R. Edge and E. Stulz, *Phys. Chem. Chem. Phys.*, 2013, **15**, 10930–41.
46 J. Jeener, *Advances in Magnetic Resonance, Vol. 10*, Academic Press, New York, 1982, vol. 10, pp. 1–48.
47 J. Kowalewski and L. Mäler, *Nuclear Spin Relaxation in Liquids: Theory, Experiments, and Applications*, Taylor & Francis Group, New York, U.S.A., 2006.
48 M. H. Levitt, *Annu. Rev. Phys. Chem.*, 2012, **63**, 89–105.
49 E. B. Wilson Jr., C. C. Lin and D. R. Lide Jr., *J. Chem. Phys.*, 1955, **23**, 136–142.
50 T. Helgaker, M. Jaszuński and K. Ruud, *Chem. Rev.*, 1999, **99**, 293–352.
51 E. Ilisca and K. Bahloul, *Phys. Rev. A*, 1998, **57**, 4296–4300.
52 A. L. Fetter and J. D. Walecka, *Theoretical Mechanics of Particles and Continua*, Dover Publications, Inc., New York, U.S.A., 2003.
53 C. Eckart, *Phys. Rev.*, 1935, **47**, 552–558.
54 J. D. Louck and H. W. Galbraith, *Rev. Mod. Phys.*, 1976, **48**, 69–106.
55 P. R. Bunker and P. Jensen, *Molecular Symmetry and Spectroscopy*, NRC Reserch Press, Otawa, 2nd edn, 2006.
56 *The TCF formulas were computed with the SpinDynamica code for Mathematica, programmed by Malcolm H. Levitt, with contributions from Jyrki Rantaharju, Andreas Brinkmann, and Soumya Singha Roy, available at <www.SpinDynamica.soton.ac.uk>. The author is greatful for advise from Prof. M. H. Levitt to get a compact form of SR-TCF*.
57 G. Pileio and M. H. Levitt, *J. Magn. Reson.*, 2007, **187**, 141–5.
58 E. Belorizky, P. H. Fries, L. Helm, J. Kowalewski, D. Kruk, R. R. Sharp and P.-O. Westlund, *J. Chem. Phys.*, 2008, **128**, 052315.
59 D. Kruk, *Theory of Evolution and Relaxation of Multi-Spin Systems: Application to Nuclear Magnetic Resonance (NMR) and Electron Spin Resonance (ESR)*, Arima Publishing UK, Burry St Edmunds, 2007.
60 P.-O. Westlund, *Dyn. Solut. Fluid Mix. by NMR*, John Wiley and Sons Ltd, Singapore, 1994, ch. 4, pp. 174–229.
61 D. M. Brink and G. R. Satchler, *Angular Momentum*, Oxford University Press, Oxford, 3rd edn, 1994.
62 K. Aidas, C. Angeli, K. L. Bak, V. Bakken, R. Bast, L. Boman, O. Christiansen, R. Cimiraglia, S. Coriani, P. Dahle, E. K. Dalskov, U. Ekström, T. Enevoldsen, J. J. Eriksen, P. Ettenhuber, B. Fernández, L. Ferrighi, H. Fliegl, L. Frediani, K. Hald, A. Halkier, C. Hättig, H. Heiberg, T. Helgaker, A. C. Hennum, H. Hettema, E. Hjertenæs, S. Høst, I. M. Høyvik, M. F. Iozzi, B. Jansík, H. J. A. Jensen, D. Jonsson, P. Jørgensen,

J. Kauczor, S. Kirpekar, T. Kjærgaard, W. Klopper, S. Knecht, R. Kobayashi, H. Koch, J. Kongsted, A. Krapp, K. Kristensen, A. Ligabue, O. B. Lutnæs, J. I. Melo, K. V. Mikkelsen, R. H. Myhre, C. Neiss, C. B. Nielsen, P. Norman, J. Olsen, J. M. H. Olsen, A. Osted, M. J. Packer, F. Pawlowski, T. B. Pedersen, P. F. Provasi, S. Reine, Z. Rinkevicius, T. A. Ruden, K. Ruud, V. V. Rybkin, P. Sałek, C. C. M. Samson, A. S. de Merás, T. Saue, S. P. A. Sauer, B. Schimmelpfennig, K. Sneskov, A. H. Steindal, K. O. Sylvester-Hvid, P. R. Taylor, A. M. Teale, E. I. Tellgren, D. P. Tew, A. J. Thorvaldsen, L. Thøgersen, O. Vahtras, M. A. Watson, D. J. D. Wilson, M. Ziolkowski and H. Ågren, *WIREs Comput Mol Sci 2014*, 2014, **4**, 269–284.

63 D. A. Case, T. A. Darden, T. E. Cheatham, C. L. Simmerling, J. Wang, R. E. Duke, R. E. Luo, R. C. Walker, W. Zhang, K. M. Merz, B. Roberts, S. Hayik, A. Roitberg, G. Seabra, J. Swails, A. W. Götz, I. Kolossváry, K. F. Wong, F. Paesani, J. Vanicek, W. R. M, J. Liu, X. Wu, S. R. Brozell, T. Steinbrecher, H. Gohlke, Q. Cai, X. Ye, M.-J. Hsieh, G. Cui, D. R. Roe, D. H. Mathews, M. G. Seetin, R. Salomon-Ferrer, C. Sagui, V. Babin, T. Luchko, S. Gusarov, A. Kovalenko and P. A. Kollman, *AMBER 12, University of California, San Francisco*, 2012.

64 J.-H. Choi and M. Cho, *J. Chem. Theory Comput.*, 2011, **7**, 4097–4103.

65 R. C. Walker, M. F. Crowley and D. A. Case, *J. Comput. Chem.*, 2007, **29**, 1019.

66 J. W. Caldwell and P. A. Kollman, *J. Phys. Chem.*, 1995, **99**, 6208–6219.

67 T. Fox and P. A. Kollman, *J. Phys. Chem. B*, 1998, **102**, 8070–8079.

68 *The author acknowledges the use of the IRIDIS High Performance Computing Facility, and associated support services at the University of Southampton, in the completion of this work.*

69 J. Gauss, K. Ruud and T. Helgaker, *J. Chem. Phys.*, 1996, **105**, 2804–2812.

70 A. M. Teale, O. B. Lutnæs, T. Helgaker, D. J. Tozer and J. Gauss, *J. Chem. Phys.*, 2013, **138**, 024111.

71 K. Ruud, T. B. Demissie and M. Jaszuński, *J. Chem. Phys.*, 2014, **140**, 194308.

72 N. A. C. Cressie, *Statistics for Spatial Data*, John Wiley and Sons, Inc., revised edn, 1993, p. 928.

73 K. Elsayed and C. Lacor, *Appl. Math. Comput.*, 2014, **236**, 325–344.

74 D. R. Jones, C. D. Perttunen and B. E. Stuckman, *J. Optim. Theory Appl.*, 1993, **79**, 157–181.

75 E. Anderson, Z. Bai, C. Bischof, S. Blackford, J. Demmel, J. Dongarra, J. Du Croz, S. Greenbaum, A. Hammarling, A. McKenney and D. Sorensen, *LAPACK Users' Guide*, Society for Industrial and Applied Mathematics, Philadelphia, PA, 3rd edn, 1999.

76 A. I. Forrester and A. J. Keane, *Prog. Aerosp. Sci.*, 2009, **45**, 50–79.

77 Y. Yuan, M. J. L. Mills and P. LA Popelier, *J. Mol. Model.*, 2014, **20**, 2172.

78 P. Audze and V. Eglais, *Probl. Dyn. Strength*, Zinatne Publishing House, Riga, 1977, pp. 104–107.

79 M. Holz, X.-a. Mao, D. Seiferling and A. Sacco, *J. Chem. Phys.*, 1996, **104**, 669.

80 C. J. Jameson, A. K. Jameson, J. K. Hwang and N. C. Smith, *J. Chem. Phys.*, 1988, **89**, 5642–5649.

81 P. E. Kloeden and E. Platen, *Numerical Solution of Stochastic Differential Equations*, Springer-Verlag, Berlin, 1992.

82 W. H. Press, S. A. Teukolsky, W. T. Vetterling and B. P. Flannery, *Numerical Recipes in C: The Art of Scientific Computing*, Cambridge University Press, New York, 2nd edn, 1992.

83 Y. Zhang, X. Duan, P. C. Soon, V. Sychrovský, J. W. Canary and A. Jerschow, *ChemPhysChem*, 2016, **6**, 1–6.